Calibrated analysis framework for nanopore direct RNA sequencing uncovers cell-specific m^{6}A stoichiometry at conserved sites

Authors

Denise Ohnezeit*[1], Elene Loliashvili*[2], Gregory Putzel[3], Ruth Verstraten[2,4], Jianheng Liu[5], Luke S. Nicholson[5], Alejandro Pironti[3], Samie R. Jaffrey[5], Daniel P. Depledge[#1,2,4,6], Angus C. Wilson[#1]

Affiliations

[1]Department of Microbiology, New York University School of Medicine, New York, NY, USA

[2]Institute of Virology, Hannover Medical School, Hannover, Germany

[3]Antimicrobial-Resistant Pathogens Program, New York University Grossman School of Medicine, New York, NY, USA

[4]German Center for Infection Research (DZIF), partner site Hannover-Braunschweig, Hannover, Germany

[5]Department of Pharmacology, Weill Medical College, Cornell University, New York, NY, USA

[6]Cluster of Excellence RESIST (EXC 2155), Hannover Medical School, Carl-Neuberg-Straße 1, 30625 Hannover, Germany

* Joint first authors: contributed equally

[#] Joint senior authors: contributed equally

ORCIDs

DO = 0000-0002-2346-2545

EL = 0009-0006-4098-5010

GP = 0000-0002-5211-2608

RV = 0009-0008-6046-6335

JL = 0000-0003-0216-1951

LSN = 0009-0005-8203-7249

AP= 0000-0002-7759-6776

SRJ = 0000-0003-3615-6958

DPD = 0000-0002-4292-0599

ACW = 0000-0002-5016-4164

Abstract

Nanopore direct RNA sequencing (DRS) coupled with Dorado modification-aware basecalling enables mapping of epitranscriptomic modifications including N^6-methyladenosine (m^6A) at the level of individual RNAs. However, a lack of systematic benchmarking continues to raise questions regarding the sensitivity, specificity, and reproducibility of this method. To address this and to establish a best-practice workflow, we evaluated multiple Dorado versions using *in vitro* transcribed RNA and an m^6A methyltransferase inhibitor as specificity controls. We established that stringent filtering is necessary to reduce false-positive calls and found strong concordance at high-stoichiometry sites when compared to an orthogonal m^6A mapping method (GLORI). Further, by applying DRS to human primary fibroblasts and HD10.6 neurons, we uncovered cell type-specific differences in m^6A stoichiometry, indicating a finely tuned epitranscriptomic regulation. Our study thus presents the first systematic comparison of Dorado and GLORI from the same input RNA and expands characterization of the m^6A epitranscriptome to fibroblasts and neurons.

Introduction

Epitranscriptomics describes the occurrence of chemical modifications on RNA that regulate stability, localization, splicing, translation or decay (Gilbert and Nachtergaele 2023). To date, over 170 RNA modifications are known to occur across all classes of RNA including eukaryotic mRNA (Cappannini et al. 2023). Of these, at least thirteen different chemical modifications have been characterized in mRNAs, comprising both cap-proximal and internal modifications (Anreiter et al. 2021). By contrast, current evidence indicates that lncRNAs harbor a more limited repertoire of modifications, primarily N^6-methyladenosine (m^6A), 5-methylcytosine (m^5C), and N7-methylguanosine (m^7G) (Yang et al. 2024a). One of the best studied and most abundant internal mRNA modifications is m^6A. Functional studies of m^6A methylases, demethylases and m^6A binding proteins, as well as sequencing-based mapping methods have increased our understanding of m^6A as a reversible and dynamic modification that fine-tunes nearly all

aspects of mRNA metabolism (Zaccara et al. 2019; He and He 2021; Murakami and Jaffrey 2022; Gilbert and Nachtergaele 2023; Sendinc and Shi 2023).

In addition to m^6A, other widespread and functionally important marks include m^5C, which is less abundant but influences mRNA export and stability, pseudouridine (Ψ), which contributes to mRNA stability, translation and splicing, and adenosine-to-inosine (A to I) editing, which is involved in splicing, stability and recoding events that contribute to protein diversity (Sun et al. 2023).

Techniques based on short-read (Illumina) sequencing have advanced in recent years to achieve single-nucleotide resolution and quantitative mapping of RNA modifications. The approaches that have emerged to map m^6A can be broadly classified as antibody-based, enzyme-assisted or chemical conversion methods (Moshitch-Moshkovitz et al. 2024).

Early antibody-based techniques (Dominissini et al. 2012; Meyer et al. 2012; Linder et al. 2015) provided the first transcriptome-wide insights into m^6A architecture, albeit at limited resolution. Enzyme-assisted methods (Meyer 2019; Xiao et al. 2023) have improved precision but can introduce enzymatic biases. These biases are avoided with GLORI-Sequencing (GLORI), which selectively deaminates unmethylated adenosines, enabling theoretically unbiased, quantitative, single-nucleotide mapping of m^6A (Liu et al. 2023).

Despite advances, the broad utility of these approaches is limited by a lack of isoform specificity, as well as biases associated with amplification, specificity of antibodies or variable adenosine conversion rates (Diensthuber and Novoa 2025). Oxford Nanopore Technologies (ONT) direct RNA sequencing (DRS) offers an alternative to these methods by analyzing native RNA molecules that have retained their modifications (Garalde et al. 2018). As single RNAs pass through nanopores, signal changes are interpreted to determine canonical and modified residues at single-nucleotide resolution on individual transcripts (Jain et al. 2016; Viehweger et al. 2019). For the now discontinued DRS SQK-RNA002 chemistry used with R9 flowcells, multiple research groups developed algorithms for detecting RNA modifications. These methods can be divided into error rate-based and current signal-based (Abebe et al. 2022). While the recent release of the DRS SQK-RNA004 chemistry and RNA-specific flowcells reduced the utility of many of these tools, introduction of a modification-aware basecaller (Dorado) provides an all-in-one toolkit for basecalling, RNA modification detection, and poly(A) tail length estimation. Early versions of Dorado (e.g. v0.5.0 and v0.6.0) enabled m^6A (DRACH-context only) detection, while version v0.7.0 enabled detection of Ψ and all-

83 context m^6A. More recent versions (v0.8.0 and v0.9.0) allow both DRACH- and all-context m^6A detection,
84 together with Ψ, inosine and m^5C (Zou et al. 2025).

85 In a recent overview of this emerging technology, Cruciani and Novoa highlighted the importance of
86 rigorous evaluation of the limitations of Dorado and advocated forcefully for the establishment of best
87 practices to ensure consistency and accuracy going forward (Cruciani et al. 2025). To date, only a handful
88 of studies of this kind have been published. A series of studies from Novoa and colleagues showed that
89 Dorado performs robustly on synthetic modified and unmodified RNA molecules but also found that
90 overlaps in the identification of specific modifications and false-positive calls remain a challenge but can
91 be mitigated by the inclusion of *in vitro* transcribed (IVT) controls (Cruciani et al. 2025; Diensthuber and
92 Novoa 2025). Independently, Esfahani and colleagues used poly(A) RNA from a B-lymphocyte cell line to
93 compare SQK-RNA002 and SQK-RNA004-derived DRS data. While they concluded that Dorado
94 outperformed other RNA modification detection tools, IVT controls were necessary to reduce false-
95 positive calls (Esfahani et al. 2025). Recent benchmarking efforts comparing Dorado and m6Anet on SQK-
96 RNA004 chemistry have shown that both tools achieve high recall and strong stoichiometry correlations
97 at DRACH motifs but exhibit higher false discovery rates on IVT controls and lower recalls of low-
98 stoichiometry genomic m^6A sites. However, these evaluations relied on previously published GLORI and
99 eTAM-Seq datasets, rather than matched input material (Diensthuber and Novoa 2025; Zou et al. 2025).
100 By directly comparing m^6A detection by DRS coupled with Dorado and GLORI on the same RNA inputs, our
101 study overcomes this limitation. Specifically, we systemically benchmark multiple versions of Dorado using
102 poly(A) RNA from primary (normal) human dermal fibroblasts (NHDFs) and functional human neurons
103 produced through terminal differentiation of HD10.6 cells (Raymon et al. 1999), along with IVT RNA. We
104 included treatments with STM2457, an enzymatic inhibitor of the primary m^6A methyltransferase METTL3
105 (Yankova et al. 2021), to robustly assess false-positive m^6A detection rates and also compared the DRS
106 outputs with those obtained from GLORI (Yang et al. 2024b) using the same RNA as input. While our
107 analysis is centered on the sensitivity and specificity of m^6A detection in DRS datasets, we also benchmark
108 the ability of Dorado to reliably detect m^5C, Ψ, and inosine. Together, our data provides a robust workflow
109 for DRS-based modification detection that reliably captures transcriptome-wide, isoform-level, site-
110 specific stoichiometries of RNA modifications.By expanding m^6A mapping on primary human fibroblasts
111 and functional human neurons, we uncover mostly conserved m^6A profiles but reveal increased site-
112 specific m^6A stoichiometries in neuronal cells.

113

114 # Results

115 **Systematic benchmarking of ONT's Dorado across human cell types.**

116 To evaluate the performance of ONT's basecalling tool Dorado across different human cell types, we
117 selected primary NHDFs and differentiated HD10.6 cells as a neuron-like model. Prior to isolation of total
118 RNA, cells were treated for 48h with a small molecule inhibitor of METTL3 (STM2457) or with vehicle
119 (DMSO). We then isolated poly(A) RNA and subjected the same input material to both DRS and GLORI. The
120 same material was also used to generate IVT RNA (**Fig. 1A**). Dorado basecalling using version v.0.9.0
121 resulted in over 13M reads using poly(A) RNA from NHDFs treated with DMSO or STM2457, while we
122 obtained over 5M and 10M reads from DMSO- and STM2457-treated HD10.6 cells, respectively. The rate
123 of primary alignment to the human genome (hg38) was over 98% for all the sequenced samples. A detailed
124 overview of read statistics generated by DRS can be found in **Supplementary Table 1**.

125 To systematically benchmark Dorado, we performed basecalling using versions v0.5.0 through v0.9.0.
126 Reads were aligned to the human genome and transcriptome to obtain comprehensive information on
127 isoform-level modification detection. Further, we explored different aspects of detected modifications
128 using the outputs generated by ONT's Modkit tool. We assessed multiple filtering strategies using base
129 and modification probabilities, as well as stoichiometry distributions, and evaluated them based on the
130 IVT data and sensitivity to METTL3 inhibition. By filtering out false-positive calls using multiple control
131 layers, we determined high-confidence m^6A sites (**Fig. 1B**). Finally, we compared these high-confidence
132 predictions with sites identified by GLORI performed on the same input RNA. Using these results, we
133 developed a benchmarked pipeline that filters m^6A sites predicted by Dorado to minimize false-positive
134 detection without impacting sensitivity (**Fig. 1C**).

135 **Stringent filtering of modification probabilities removes false positives**

136 During modification-aware basecalling, each nucleotide is assigned a basecall probability score ranging
137 from 0 to 1. Similarly, individual modified nucleotides are assigned a modification probability score in the
138 same range. To establish a baseline for false-positive m^6A predictions, we plotted basecall and modification
139 probability distributions for an IVT poly(A) RNA dataset processed using Dorado v0.9.0 and aligned to
140 human genome (**Fig.2**). We binned basecall and modification probability values for A and m^6A (all-context
141 and DRACH) and compared this data from DMSO- and STM2457-treated NHDF datasets.

142 We observed that 75-90% of A basecalls (in all datasets) have probability scores above 0.8 **(Fig. S1A)**. Since
143 all A bases are considered during all-context m^6A calling, the fraction of m^6A sites is substantially smaller
144 when compared to DRACH-context m^6A sites (**Fig.2A,B, Fig.S1B,C**). The modification probability
145 distributions are effectively identical for DMSO-treated, STM2457-treated and IVT datasets below 0.98,
146 while the profiles differ substantially at probabilities ≥ 0.98. This suggests that sites detected below 0.98
147 are likely false positives, indicating that only high-probability m^6A calls can be considered reliable. Here,
148 STM2457 treatment shows a marked reduction in the number of reported m^6A sites in both all-context
149 and DRACH-only datasets when compared to the DMSO treatment (**Fig. 2A,B**).

150 In addition to m^6A, we examined modification probability distributions for Ψ, inosine and m^5C, each of
151 which can be basecalled with Dorado v0.9.0 (**Fig. S2**). For Ψ and I, the modification probability distributions
152 for the STM2457 and DMSO datasets only diverge from the IVT dataset at ≥ 0.99 modification probability,
153 thus providing a relevant threshold for filtering out false positives (**Fig. S2A,B**). By contrast, m^5C
154 modification probability distributions were similar between all three datasets and no filter could be
155 adequately established (**Fig. S2C**). While this likely reflects a low rate of m^5C installation, it also indicates
156 that the m^5C model utilized by Dorado requires further refinement.

157 Modification probability distributions have similar profiles for transcriptome-aligned NHDF data (**Fig. S3)**
158 as well as genome- and transcriptome-aligned data from HD10.6 cells **(Fig. S4, Fig. S5**). Of note, the fraction
159 of high-probability inosine sites is increased in STM2457-treated cells, compared to DMSO-treated ones
160 in genome-aligned data (**Fig. S2B, Fig.S4D**), which points to increased numbers of retained introns in the
161 METTL3-inhibited sample. Accordingly, this effect is absent in transcriptome-aligned data (**Fig. S3D, Fig.**
162 **S5D**).

163 While IVT transcriptomes serve as excellent negative controls, we also considered whether the RNA
164 calibration strand (RCS) that is added during DRS library preparation could serve a similar function. The
165 RCS is a synthetic Enolase II RNA derived by IVT[13] that, similarly to the IVT transcriptomes, are devoid of
166 RNA modifications. Despite the reduced diversity of sequence in the RCS data, the overall results were
167 comparable to that from the IVT transcriptome data (**Fig. S6A,B, Fig. 2A,B**), demonstrating that the RCS
168 can be used as a "built-in" negative control for modification detection with DRS. Finally, we determined
169 that basecall and modification probability distributions remain generally consistent between Dorado
170 versions although more m^6A and Ψ sites are detected with high modification probability in Dorado versions
171 v0.8.0/v0.9.0 compared to v0.7.0 (**Fig. S6C-E)**.

172 **Filtering by stoichiometry further eliminates potential false positives**

173 We next examined the stoichiometry distributions for all m^6A sites in both unfiltered and filtered NHDF
174 datasets (**Fig. S7**). Here, unfiltered datasets showed that the vast majority of m^6A sites, 92% for all-context
175 and 75% for DRACH-context, have stoichiometry values < 10% with less than 1% sites showing high (> 50%)
176 stoichiometry. Application of our filtering strategy removed over 70% of the sites (**Fig. 2E)**, regardless of
177 the context, almost all of which showed stoichiometries of < 10%, without significantly changing the
178 numbers of high stoichiometry sites detected (**Fig. S7**). A similar analysis of the IVT transcriptome revealed
179 large numbers of false positive m^6A sites with stoichiometry values below 10%, most of which were
180 eliminated by application of our filters (**Fig. S8A,B**). However, the remaining presence of low stoichiometry
181 false-positive sites indicates that an additional layer of filtering to exclude sites with < 10% stoichiometry
182 is beneficial. An additional argument in support of our modification probability filtering strategy is the
183 observation that treatment with the METTL3 specific inhibitor STM2457 dramatically reduced m^6A
184 installation at sites with ≥ 10% stoichiometry in untreated datasets in a context-independent manner (**Fig.
185 2C,D, Supplementary Table 2**). Similar results were observed for the transcriptome aligned NHDF and
186 HD10.6 m^6A stoichiometry distributions as well (**Fig. S9, Fig. S10, Supplementary Table 2**).

187 To determine whether our filtering strategy could be applied to other RNA modifications detected by
188 Dorado, we generated stoichiometry distributions for Ψ and inosine in unfiltered and filtered (≥ 0.99
189 modification probability) human genome-aligned DMSO- and STM2457-treated NHDFs and HD10.6s. As
190 with m^6A (**Fig. S7**), 92% of detected Ψ and 96% of inosine have less than 10% stoichiometry (**Fig. S11, Fig.
191 S12)**. A recent study that explores Ψ in human mRNAs using 2-bromoacrylamide-assisted cyclization
192 sequencing (BACS) corroborates our results, showing that 82% of Ψ modifications are detected at low
193 levels (below 20%) (Xu et al. 2024).

194 Above 10% stoichiometry, in our data, there are more inosine sites in STM2457-treated cells than DMSO-
195 treated cells, reflected also in the stoichiometry distributions (**Fig. S11, Fig. S12, Supplementary Table 2**).
196 Ψ and inosine stoichiometry distributions in our IVT data **(Fig.S8C,D)** further validates our filtering strategy
197 of ≥ 0.99 modification probability, as it substantially reduces the number of detected false-positive sites in
198 the unfiltered data even at higher (> 50%) stoichiometries in case of inosine (**Fig.S8D**).

199 We have thus demonstrated that setting thresholds for basecall modification probabilities provides a
200 robust method for identifying and filtering false-positive modification calls. For the purposes of this study,

201 we further evaluated the effect of placing the modification threshold on the modification data and
202 restricted the downstream analyses to m^6A sites with probability scores ≥ 0.98.

203 **RNA modification detection rates differ between Dorado versions**

204 Dorado basecalling relies on models generated using Remora (github.com/nanoporetech/remora) that are
205 frequently updated. This raises an important question as to whether these updates produce notably
206 different outputs that could impact biological interpretation. To address this, we utilized multiple Dorado
207 versions and Remora models to perform modification calling of our NHDF dataset. We restricted our
208 analyses to m^6A and Ψ as these are the only modifications that could be detected in previous versions.
209 Here, we observe that m^6A and Ψ stoichiometry distributions are generally consistent between different
210 Dorado versions (**Fig. S13**), albeit with greater numbers of low stoichiometry (< 10%) sites detected in
211 older Dorado versions. There is a large overlap of the detected ≥ 10%-stoichiometry m^6A (DRACH and all-
212 context) and Ψ sites between versions, although there are a lot of unique all-context m^6A and Ψ sites
213 identified with just v0.7.0 and not v0.8.0-v0.9.0, that are reduced after applying our modification
214 probability filter (**Fig. S14A,B**). Ψ sites uniquely detected with different versions are found in slightly
215 different sequence contexts (**Fig. S14C,D**). Thus, while RNA modification detection with Dorado is sensitive
216 to changes in the underlying models/versions, this can be effectively controlled through the application of
217 filters that only retain sites with high-confidence modification probability calls.

218 **GLORI exhibits reduced specificity but converges with Dorado predictions at high stoichiometry sites**

219 To assess the agreement of DRS Dorado-derived predictions with an orthogonal m^6A detection method,
220 we conducted GLORI on the same NHDF RNA preparations. To ensure a fair comparison of m^6A sites across
221 the two methods, we applied the following filtering strategies: For Dorado (DRACH model), this included
222 thresholds on modification probability (A ≥ 0.8, m^6A ≥ 0.98) and read coverage (≥ 20). For GLORI, we used
223 filters based on coverage (≥ 20) and statistical significance (p-value ≤ 0.05). Next, we extracted m^6A sites
224 that were present in both DMSO and STM2457 treated samples and removed all sites with ≤ 10%
225 stoichiometry in DMSO (**Fig. 3A**). This stepwise strategy reduced false positives and enabled a fair
226 comparison of the high confidence m^6A sites identified by both approaches.

227 As shown in the violin plots, both the all-context and DRACH-context Dorado models identify similar
228 numbers of m^6A sites (81,012 (all-context model) and 72,372 (DRACH model)), the stoichiometries of
229 which were strongly reduced upon STM2457 treatment (**Fig. 3B**). When we analyzed the motifs of the m^6A
230 sites detected with the all-context model, we observed nearly 9,000 sites outside of DRACH motifs.

231 Importantly, the total number of m^6A sites within DRACH motifs was nearly identical to the number of m^6A
232 sites reported using the DRACH model (**Fig.3B**). Unexpectedly, GLORI detects a substantially higher
233 number of sites when using all motifs (140,934) compared to DRACH motifs alone (27,926) (**Fig. 3C**). The
234 fact that most GLORI-identified sites fall outside DRACH motifs suggests these are false positives. This
235 interpretation is reinforced by the observation that the overlap between Dorado and GLORI datasets
236 remains virtually unchanged when comparing GLORI "all motif" and "DRACH motifs" (n=13,614) site sets,
237 underscoring that the additional non-DRACH sites in GLORI (n= 113,008) are largely spurious (**Fig. S15A**).

238 We obtained similar results when comparing m^6A sites obtained with Dorado and GLORI from HD10.6
239 cells. Overall, we detected a similar number of m^6A sites in HD10.6 cells using the all-context and DRACH-
240 specific Dorado models (77,728 and 67,222, respectively) (**Fig. S15B**). By contrast, we detected 174,282 vs
241 27,965 m^6A sites using GLORI without or with DRACH filtering, respectively (**Fig. S15C**).

242 To evaluate how stoichiometry thresholds affect the agreement between GLORI and Dorado, we compared
243 the overlap of high-confidence GLORI-identified sites with Dorado m^6A (DRACH context) calls across
244 increasing m^6A stoichiometry cutoffs (**Fig. 3D**). At the lowest stoichiometry threshold applied (≥ 10%),
245 13,614 sites overlapped, representing less than half (48.8%) of GLORI sites. However, as the stringency
246 increased, the relative overlap increased sharply: at ≥ 20%, nearly 70% of GLORI sites overlapped (11,536
247 sites), at ≥ 50% almost 90% overlapped (6,307 sites), and at the highest cutoff (≥ 80%), over 93% of GLORI
248 sites (3,119 sites) were also detected by Dorado. These results demonstrate that while GLORI detects a
249 broad set of potential m^6A sites, only the sites with high stoichiometries overlap with Dorado, indicating
250 high signal to noise ratios in the GLORI datasets.

251 GLORI relies on the high-efficiency conversion of adenosine to inosine with overall gene A to I conversion
252 rates needing to exceed 95-98% (Xu et al. 2024; Xie et al. 2025). Similarly, we observed the conversion
253 rates for our NHDF and HD10.6 datasets to be 95% (Supplementary **Table 3**), but we found that small
254 variations in gene conversion rates can strongly influence the sensitivity and specificity of GLORI, as only
255 high-stoichiometry m^6A sites overlapped with DRS-derived predictions (**Fig. 3D**).

256 **DRS coupled with Dorado outperforms GLORI in isoform-specific m^6A detection**

257 Next, we wanted to highlight the advantage of long-read sequencing in terms of mapping reads with
258 isoform-precision to the human transcriptome, which is not possible using GLORI due to its reliance on
259 short-read sequencing. We first confirmed that mapping Dorado-basecalled sites to the human
260 transcriptome results in the detection of similar numbers of m^6A sites in both NHDFs and HD10.6 cells (**Fig.**

261 **S15D,E**). To assess if DRS coupled with Dorado identifies distinct m^{6}A profiles on different transcript
262 isoforms, we analyzed the *SPEN* gene locus which was previously shown to contain more than 100 m^{6}A
263 sites (Liu et al. 2023). On a genomic level, we detected 42 m^{6}A sites using DRS, while GLORI only detected
264 5 m^{6}A sites (**Fig. 3E**). Out of the 7 total isoforms of *SPEN*, *SPEN-201* and *SPEN-202* were detectable in DRS-
265 derived data, considering a minimal coverage of 20 (**Supplementary Table 4**). When plotting the m^{6}A sites
266 detected by transcriptome-aligned DRS data, we found that the *SPEN-201* isoform exhibited more m^{6}A
267 sites, albeit with a lower median stoichiometry compared to the *SPEN-202* isoform (**Fig. 3F**). This example
268 highlights that DRS is superior compared with GLORI for isoform-level m^{6}A quantification.

269 **Dorado profiling reveals cell type differences in m^{6}A distribution and stoichiometry**

270 To assess the reproducibility of Dorado across DRS datasets derived from different cell types, we compared
271 the m^{6}A methylomes of NHDFs and HD10.6 cells. To ensure a fair comparison, we extracted genes that
272 were expressed in both cell types. Next, we compared the total numbers of high confidence m^{6}A sites in
273 NHDFs and HD10.6 cells within the genes expressed in both cell types and found that 87% of HD10.6-
274 derived m^{6}A sites overlap with those detected in NHDFs (**Fig. 4A**). Site-specific m^{6}A stoichiometries from
275 the shared gene set correlated strongly across cell types (Pearson r = 0.93), although we observed a global
276 shift in the HD10.6 dataset, where m^{6}A stoichiometries were generally higher than in NHDFs (**Fig. 4B**).
277 Plotting the m^{6}A stoichiometry distributions of the 38,217 m^{6}A sites shared between both cell types
278 showed a strong increase in the median m^{6}A stoichiometry of HD10.6 cells (70.2%), compared to NHDFs
279 (54%) (**Fig. 4C**).

280 We next aimed to conduct a comparative motif analysis of m^{6}A sites detected in NHDFs and HD10.6 cells.
281 Sequence logos confirmed strong enrichment of the canonical DRACH consensus motif for both cell types
282 in modification probability-filtered data, with the GGACU pentamer being the most prominent (**Fig. 4D,E,**
283 **Fig.S16**). Quantification of 5-mer distributions revealed highly similar motif preferences across datasets.
284 While the global motif architecture of m^{6}A deposition is conserved between NHDFs and HD10.6 cells, we
285 observed a trend toward higher stoichiometries in the HD10.6 dataset, particularly within the most
286 abundant DRACH motifs, suggesting enhanced modification efficiency in the neuron-like context (**Fig. 4F,**
287 **G**).

288 Metagene analysis showed, as known previously, that m^{6}A is enriched near the stop codons and in the 3'
289 UTRs (**Fig. S17A**). Several studies have examined the relationship between exon architecture and m^{6}A
290 distribution on mRNAs[1,2,3], and so we also examined m^{6}A sites in monoexonic transcripts separately and

291 found that monoexonic transcripts are more broadly m^6A-modified across entire CDS (**Fig. S17A**). m^6A
292 (both all-context and DRACH-context) distribution profiles look less typical for all-stoichiometry or ≤ 10%
293 stoichiometry sites in both NHDF and HD10.6 datasets (**Fig. S17B+C**). For all-context m^6A (**Fig. S17B**),
294 modification filter also proves to be deciding for the distribution profile, together with ≥ 10%
295 stoichiometry.

296 To connect shared m^6A sites with their functional context and illustrate their distribution on individual
297 transcripts, we conducted a KEGG pathway analysis with the genes that contain shared m^6A sites between
298 NHDFs and HD10.6 cells. We observed a significant enrichment in pathways related to neurodegeneration,
299 infection, and intracellular signaling, including axon guidance and mTOR signaling (**Fig. 4H**). To further
300 illustrate these findings, we examined representative genes contained in one or more of these pathways.
301 *WNTB5*, *MAPK1*, *AKT1*, *NCK1* and *NRP1* all showed robust methylation in both NHDFs and HD10.6 cells,
302 with consistently higher stoichiometries observed in the neuronal-like context. In contrast, *ACTG1*,
303 included as a housekeeping control not represented in the enriched pathways, displayed stable and
304 comparatively uniform methylation across both cell types (**Fig. 4I**).

305 Together, these results demonstrate that while the global architecture of m^6A deposition is largely
306 conserved between primary fibroblasts and neuronal-like cells, but unexpectedly the neuronal context is
307 characterized by a global shift toward higher m^6A stoichiometries. This difference is readily detectable in
308 single genes. These findings suggest that cell type-specific regulation of m^6A may fine-tune core cellular
309 pathways relevant to that cell type.

310

311 ## Discussion

312 High rates of false positives remain a major problem in epitranscriptomic mapping tools, even with the
313 advent of modification-aware basecalling models (Cruciani et al. 2025). Comparing the outputs of
314 orthogonal methods performed on the same input material, combined with use of IVT RNA and/or specific
315 methyltransferase inhibition, offers an effective mitigation strategy (Cruciani et al. 2025; Diensthuber and
316 Novoa 2025). The results presented here establish a robust framework that minimizes false positives and
317 enables isoform-specific and quantitative m^6A mapping. Through a direct comparison with GLORI, we
318 showed that combining DRS datasets with Dorado modification-aware basecalling provides greater
319 scalability, isoform resolution, and reproducibility across different cell types. Further, the simplicity of DRS
320 library preparation enhances consistency whereas GLORI is constrained by a laborious and technically

321 challenging protocol that is extremely sensitive to adenosine conversion rates (Shen et al. 2024). Despite
322 these limitations, we determined that the majority of m^6A sites in our filtered DRS datasets could be
323 confirmed by GLORI. By expanding our analysis across multiple human cell types, we further determine
324 that the sites of m^6A installation are conserved for the most part but that the stoichiometries show cell-
325 type specific differences.

326 Crucially, the inclusion of transcriptome-wide IVT datasets and the use of a selective METTL3 inhibitor
327 (STM2457) provides a robust approach to developing filters that dramatically decrease false-positive m^6A
328 detection. The impact of both approaches was readily visualized by plotting modification probability
329 distributions, enabling our determination that retaining only m^6A calls with confidence scores of 0.98 or
330 greater retained almost all STM2457-sensitive m^6A sites while eliminating the large numbers of false-
331 positive m^6A sites reported for the IVT datasets. This approach is supported by a recent study which
332 highlighted that Dorado introduces large numbers of false positives outside canonical DRACH contexts (Xie
333 et al. 2025). Our data confirms that in the unfiltered datasets, the number of false positives is higher in
334 the all-context model compared to the DRACH model. This may reflect the degenerate nature of the
335 canonical DRACH consensus and understudied differences in sequence preference between different cell
336 types and organisms. Retaining only sites at which m^6A stoichiometries exceeded 10% further reduced
337 false-positive rates while also focusing the results on identification of sites that are more likely to be
338 biologically significant. The combined effect of these filters was to provide a strong agreement between
339 the m^6A all-context and m^6A DRACH model in the detection of high confidence m^6A sites, as observed by
340 filtering for DRACH motifs from m^6A sites detected with the all-context model (**Fig.3B**).

341 Prior studies have emphasized the need for isoform-resolved m^6A quantification by demonstrating
342 widespread heterogeneity in m^6A levels between genes and their isoforms (Guo et al. 2025; Xie et al.
343 2025). Here, we showed that aligning DRS datasets to the human transcriptome reveals differential m^6A
344 installation patterns between isoforms, underscoring the importance of accurate, isoform-specific m^6A
345 quantification at single-molecule resolution and highlighting the advantage of DRS against short-read
346 sequencing approaches such as GLORI (**Fig. 3E,F**).

347 Recently, the ability of Dorado and m6Anet (Hendra et al. 2022) to identify m^6A in DRS datasets from 293T
348 and HeLa cells were systematically evaluated using IVT RNA and comparisons to published datasets
349 obtained by GLORI and eTAM-seq (Zou et al. 2025). In this case the authors found that Dorado (v0.7.2)
350 outperforms m6Anet but also advocated for the importance of applying filters to reduce false positive
351 calls. Likewise, we found that IVT RNA served as a valuable negative control to detect false positive calls.

352 Furthermore, using the RNA calibration strand (RCS) as a negative control provided a convenient and
353 simpler alternative to IVT RNA, yielding comparable probability distributions and thereby enabling a built-
354 in control for routine experiments (Viehweger et al. 2019). While m^6A detection was generally
355 reproducible across Dorado versions, model-specific differences are present, i.e. v0.7.0 produces
356 substantially more low-confidence all-context m^6A and Ψ calls than v0.8.0–0.9.0, highlighting that the
357 models remain under active development and that benchmarking should be repeated when switching to
358 a new model. Recent work further highlights that continued improvements in both nanopore sequencing
359 chemistry and basecalling models significantly enhance RNA modification detection accuracy, emphasizing
360 the importance of revisiting benchmarking and filtering strategies as models evolve (Hewel et al. 2025).

361 Focusing on other modifications that are detected by Dorado, we observe that inosine and Ψ detection
362 appears robust when applying similar filtering strategies as for m^6A, the latter supported by other studies
363 (Esfahani et al. 2025; Verstraten et al. 2025). For inosine, we observed an enrichment of high-probability
364 (> 0.99) inosine sites in genome-aligned data from STM2457-treated samples. Further studies are needed
365 to determine whether this reflects increased intron retention or misclassification of modifications by the
366 current inosine model. While DRS is the only approach that allows for robust isoform-specific m^6A
367 mapping, comparisons with orthogonal approaches remain essential to validate findings. When comparing
368 Dorado and GLORI using the same input RNA, we unexpectedly observed that only 50% of m^6A sites with
369 stoichiometries above 10% that were identified by Dorado were also present in the GLORI data although
370 increasing the stoichiometries led to increased overlap (**Fig.3D**). We attribute this to a sub-optimal gene-
371 wide adenosine conversion rate of 95% during GLORI, compared to the 98-99% rate reported in the original
372 study (Shen et al. 2024). Here, unconverted adenosines result in high signal-to-noise ratios which result in
373 lower sensitivity, explaining why the overlap with Dorado increases at higher-stoichiometry sites. This is
374 also reflected in the relatively high amount of false positive sites detected outside of DRACH motifs in the
375 GLORI datasets (**Fig. 3C**). The sensitivity of GLORI to small fluctuations thus limits its utility in comparison
376 to DRS. Whether this can be resolved with improvements to the GLORI methodology (Sun et al. 2025)
377 requires further study.

378 Prior analyses of m^6A stoichiometry distributions across immortalized human cell lines, including cancer
379 cell lines, have revealed broadly similar m^6A stoichiometry distributions (Guo et al. 2025). By contrast, our
380 analysis of primary fibroblasts (NHDFs) and neuronal cells (differentiated HD10.6 cells) revealed an overall
381 increase in m^6A stoichiometries in neurons compared to fibroblasts, especially in genes associated with
382 neuronal function. While further studies are warranted to establish the underlying mechanisms and

383 functional consequences of these differences, this aligns with the importance of m^6A in neuronal function
384 (Yu et al. 2021). This includes m^6A maps from synaptic and nuclear RNA isolated from mouse dorsal
385 hippocampus which showed that synapse-specific RNAs showed generally higher methylation levels (Sun
386 et al. 2025). Intriguingly, neuronal regulation pathways utilize differentially spliced isoforms (Su et al. 2018)
387 and a recent study revealed isoform-specific differences in m^6A sites and stoichiometries in the human
388 brain that are linked to m^6A machinery expression and cell type context (Gleeson et al. 2025).

389 In summary, using matched RNA samples from different experimental conditions and from different
390 human cell types analyzed with both Dorado and GLORI orthogonal methodologies, we establish a robust
391 pipeline for the precise and quantitative transcriptome-wide detection of m^6A in DRS datasets. Future
392 studies should aim at extending this approach using orthogonal sequencing approaches to benchmark
393 Dorado-based detection of Ψ, m^5C and inosine, as well as the newly released models for 2'O-methylation.

394

395 # Methods

396 **Cell culturing and STM2457 treatment**

397 NHDFs (Lonza) were cultured in Dulbecco's Modified Eagle Medium (DMEM, Gibco), supplemented with
398 5% heat-inactivated FBS (HI-FBS, Gibco) and 1% penicillin-streptomycin (PS, Lonza) under standard culture
399 conditions. The HD10.6 cell line was originally derived from fetal human dorsal root ganglia (DRG) and
400 immortalized by overexpression of the v-myc oncogene under tetracycline regulation. Upon addition of
401 tetracycline and neurotrophins, these cells can be differentiated into neuron-like cells that show typical
402 neuronal morphology and nociceptive properties(Raymon et al. 1999). For our experiments, we used
403 HD10.6 cells that have been matured for 10 days. For maintenance of undifferentiated HD10.6 cells (a gift
404 from Anna Cliffe, University of Virginia School of Medicine), T-75 flasks were coated with 17 µg/mL
405 fibronectin in PBS for 15 min at 37°C before adding the cell suspension. Cells were grown in Advanced
406 DMEM/F12 (Gibco), supplemented with 1x Neurocult SM1 (STEMCELL Technologies), 2 mM L-glutamine
407 (Gibco), 1x Primocin (Invivogen) and 10 ng/mL prostaglandin E1 (Sigma). 0.5 ng/mL bFGF (PeproTech) were
408 added freshly to each media change. For maturation, HD10.6 cells were seeded at a density of 25.000
409 cells/cm² in 6-well plates which were pre-coated overnight with 50 µg/mL poly-L-ornithine hydrobromide
410 (Sigma) in 0.5M borate buffer pH 8.5 (Boston Bioproducts), and 1 µg/mL fibronectin (overnight). After cell
411 attachment overnight, media was changed to Neurobasal media (Gibco), supplemented with 1x Neurocult
412 SM1, 2mM L-glutamine, 1x Primocin, 1 µg/mL doxycycline, 50 ng/mL NGF (Alomone Labs), and 25 ng/mL

413 CNTF, GDNF and NT-3 (PeproTech). Media was changed every three days until HD10.6 cells showed
414 complete neuronal morphology after 12 days. NHDFs and matured HD10.6 cells were treated with 30 µM
415 STM2457 (Sigma) or DMSO for 48h, harvested in TRIzol (Invitrogen), and stored at -80°C until RNA
416 isolation.

417 **RNA isolation**

418 RNA was extracted by the TRIzol method according to the manufacturer's instructions. Briefly, 0.2 mL
419 chloroform per 1 mL TRIzol were added and mixed by vortexing. After centrifugation for 30 min at 12,000xg
420 at 4°C, the aqueous phase was transferred to isopropanol (0.5 mL per 1 mL TRIzol), mixed and incubated
421 for 10 min at room temperature. Subsequently, the samples were centrifuged for 10 min at 12,000xg at
422 4°C and the RNA pellets were washed twice in 75% fresh ethanol. After air-drying for 5-10 min, RNA was
423 dissolved in nuclease-free H_2O and stored at -80°C until further processing. One third of each sample was
424 used for DRS and the remaining same-input material was processed for GLORI. For both DRS and GLORI,
425 poly(A) RNA was selected using the Dynabeads™ mRNA Purification Kit (Invitrogen), according to the
426 manufacturer's instructions.

427 **GLORI-Sequencing**

428 GLORI reactions were largely performed following the published protocol for RNA protection, deamination
429 and deprotection with several minor adjustments (Shen et al. 2024). Briefly, poly(A) RNA was fragmented
430 at 94°C for 2 min (NEB E6150S) and subjected to glyoxal protection, sodium-nitrite-mediated deamination
431 (750 mM $NaNO_2$ at 16°C for 8h and 4°C for 6h), and deprotection in triethylammonium acetate-formamide
432 buffer at 95°C for 10 min. Library construction was conducted using a ligation-based strategy as described
433 by Liu and colleagues incorporating 5'adapters with 11-nt UMIs (Liu et al. 2025).

434 Indexed libraries were amplified with NEBNext Dual Primers Set 2 (E7780S), purified using AMPure XP
435 beads, and validated on an Agilent TapeStation (D1000 High Sensitivity). Sequencing was performed on an
436 Illumina NovaSeq 6000 platform (150 bp paired-end mode; > 80 million reads per sample).

437 For data processing, we employed the same computational pipeline described in Liu et al (Liu et al. 2025),
438 but implemented within a Snakemake-based framework that automates the complete analysis starting
439 from raw fastq files (Köster and Rahmann 2012). Details on software versions, workflow availability, and
440 repository links are provided in the Data and code availability section below.

441 **Generation of a transcriptome-wide IVT RNA library**

We sequenced the IVT RNA from both NHDFs and HD10.6 cells along with the native poly(A) RNA to evaluate potential false-positive predictions by Dorado. This was achieved by converting the poly(A) RNA to cDNA using a poly(A) primer and a T7-incorporating strand switch primer and using the cDNA as a template for IVT synthesis.

Nanopore Sequencing of poly(A) RNA

250-300 ng of isolated poly(A) RNA and 25 ng RNA calibration strand (RCS) were used as input for the standard DRS SQK-RNA004 protocol. Resulting libraries were loaded onto individual PromethION RNA flow cells before sequencing on the PromethION 2 Solo instrument for 48h.

Nanopore basecalling

Basecalling was performed using Dorado v0.5.0, v0.6.0, v0.7.0, v0.8.0 and v0.9.0 (ONT) in super accuracy mode with modification detection enabled for m^6A (DRACH context) in v.0.5.0, 0.6.0, 0.8.0 and 0.9.0, m^6A (all context) in v0.7.0, 0.8.0 and 0.9.0, Ψ in v0.7.0, v0.8.0 and v0.9.0, and inosine and m^5C in v.0.9.0. Each dataset was processed with adapter trimming. Resulting unaligned BAM files were converted to FASTQ files containing modification tags for every read in the FASTQ read headers, using SAMtools v1.18 (Li et al. 2009) [*samtools fastq -TMM,ML*].

Genome and transcriptome level alignments

For genome-level alignment, reads were aligned against a combined human genome reference (GRCh38.p14), and the RCS gene sequence, using minimap2 v2.26 [*minimap2 -ax splice -k14 -y -uf --secondary=no*]. For transcriptome-level alignment, the reads were aligned against the human transcriptome (v47), obtained via GENCODE (Mudge et al. 2025) [*minimap2 -t 8 -ax map-ont -y -L -p 0.99*]. Using SAMtools v1.18, resulting genome- and transcriptome-aligned SAM files were converted to BAM files retaining only primary alignments [*samtools view -b -F2308* and *samtools view -b -F2324,* respectively]. BAM files were sorted [*samtools sort*] and indexed [*samtools index*].

Processing of RNA modification calls using Modkit

Probability distributions of the detected sites in human genome- and transcriptome-aligned reads were generated using sample-probs subcommand from Modkit v0.4.1 [sample-probs --hist --only-mapped --percentiles 0.1,0.2,0.3,0.4,0.5,0.6,0.7,0.8,0.85,0.9 -f 0.1]. For RCS reads -f value was increased to 0.25. The resulting .tsv files were imported into RStudio (v. 2024.12.1+563) and plotted using a custom R(v. 4.4.2)

470 script (Dorado_mod_probability_distributions.R), with the following packages: dplyr (v1.1.4), ggplot2
471 (v3.5.1), reshape2 (v1.4.4), patchwork (v1.3.0).

472 To generate extended bedMethyl files with m^6A-modified and unmodified base counts from the reads
473 mapping against the potential modification sites, we used Modkit pileup subcommand with the thresholds
474 [*--filter-threshold A:0.8 --filter-threshold T:0.8 --filter-threshold C:0.8 --filter-threshold G:0.8 --motif A 0 --*
475 *ref $REF*] with and without modification threshold filter [*--mod-thresholds a:0.98*] to generate our
476 "filtered" and "unfiltered" datasets, respectively. Canonical nucleotide calls (A, C, G, U) were retained with
477 > 80% probability scores for all modification datasets. Modification thresholds were set at 98% for m^6A
478 and 99% for all the other modifications. *--motif* was adjusted to the base for which modification status
479 was examined, which further restricted the analysis to only the positions that matched canonical
480 nucleotides in the reference genome. The resulting sites were further filtered according to the read
481 number per site (≥ 20 reads) for all the downstream analysis.

482 **Gene Ontology analysis**

483 GO analysis was performed using DAVID (Huang da et al. 2009). Genes harboring m^6A sites were filtered
484 for genes that were generally present in both datasets. Next, they were divided into NHDF-specific,
485 HD10.6-specific, and shared categories, and enrichment was assessed for biological processes. GO terms
486 were considered significant at FDR ≤ 0.05 with a minimum of 20 genes per GO term. For plotting, the top
487 20 GO terms that contained the highest gene numbers were extracted from the analysis of the shared
488 gene sets.

489 **Analysis and visualization of modification stoichiometries and distributions**

490 Stoichiometry distribution histograms and metaplots were generated using Rstudio and R v4.4.2 with the
491 following libraries: data.table, patchwork, scales, tidyr, dplyr, ggplot2[4]. Access to scripts used for analysis
492 and visualization is detailed below.

493 **Data and code availability**

494 Raw fastq and pod5 datasets generated in this study are available via the European Nucleotide Archive
495 (ENA) under the accession number PRJEB101380.

496 R scripts used in the analysis and visualization of data presented herein are available in the
497 https://github.com/DepledgeLab/HOLDEN repository.

498 The Snakemake workflow implementing the GLORI analysis pipeline is available in the
499 https://github.com/gp-micro/glori repository.

Acknowledgements and funding

DPD is supported by a German Centre for Infection Research (DZIF) Associate Professorship and the NIAID grants R01-AI170583 and R01-AI152543. DPD also receives funding from the Deutsche Forschungsgemeinschaft (DFG, German Research Foundation) under Germany's Excellence Strategy - EXC 2155, project number 390874280. EL is supported by the NIAID grant R01-AI170583 as well as the Hannover Biomedical Research School (HBRS) and the Center for Infection Biology (ZIB). DO is supported by the Walter Benjamin Programme of the DFG, project 554758329. ACW is supported by NIAID grants R01AI176335 and R01-AI170583.

References

https://github.com/nanoporetech/modkit.

Abebe JS, Verstraten R, Depledge DP. 2022. Nanopore-Based Detection of Viral RNA Modifications. *mBio* **13**: e03702-03721.

Anreiter I, Mir Q, Simpson JT, Janga SC, Soller M. 2021. New Twists in Detecting mRNA Modification Dynamics. *Trends Biotechnol* **39**: 72-89.

Cappannini A, Ray A, Purta E, Mukherjee S, Boccaletto P, Moafinejad SN, Lechner A, Barchet C, Klaholz Bruno P, Stefaniak F et al. 2023. MODOMICS: a database of RNA modifications and related information. 2023 update. *Nucleic Acids Research* **52**: D239-D244.

Cruciani S, Delgado-Tejedor A, Pryszcz LP, Medina R, Llovera L, Novoa EM. 2025. De novo basecalling of RNA modifications at single molecule and nucleotide resolution. *Genome Biology* **26**: 38.

Diensthuber G, Novoa EM. 2025. Charting the epitranscriptomic landscape across RNA biotypes using native RNA nanopore sequencing. *Mol Cell* **85**: 276-289.

Dominissini D, Moshitch-Moshkovitz S, Schwartz S, Salmon-Divon M, Ungar L, Osenberg S, Cesarkas K, Jacob-Hirsch J, Amariglio N, Kupiec M et al. 2012. Topology of the human and mouse m6A RNA methylomes revealed by m6A-seq. *Nature* **485**: 201-206.

Esfahani NG, Stein AJ, Akeson S, Tzadikario T, Jain M. 2025. Evaluation of Nanopore direct RNA sequencing updates for modification detection. *bioRxiv* doi:10.1101/2025.05.01.651717.

Garalde DR, Snell EA, Jachimowicz D, Sipos B, Lloyd JH, Bruce M, Pantic N, Admassu T, James P, Warland A et al. 2018. Highly parallel direct RNA sequencing on an array of nanopores. *Nat Methods* **15**: 201-206.

Gilbert WV, Nachtergaele S. 2023. mRNA Regulation by RNA Modifications. *Annu Rev Biochem* **92**: 175-198.

Gleeson J, Madugalle SU, Wan CY, McLean C, Bredy TW, De Paoli-Iseppi R, Clark MB. 2025. Isoform-level profiling of m(6)A epitranscriptomic signatures in human brain. *Sci Adv* **11**: eadp0783.

Guo W, Ren Z, Huang X, Liu J, Shao J, Ma X, Wei C, Cun Y, He J, Zhang J et al. 2025. Single-molecule m6A detection empowered by endogenous labeling unveils complexities across RNA isoforms. *Molecular Cell* doi:https://doi.org/10.1016/j.molcel.2025.01.014.

He PC, He C. 2021. m(6) A RNA methylation: from mechanisms to therapeutic potential. *Embo j* **40**: e105977.

Hendra C, Pratanwanich PN, Wan YK, Goh WSS, Thiery A, Göke J. 2022. Detection of m6A from direct RNA sequencing using a multiple instance learning framework. *Nature Methods* **19**: 1590-1598.

Hewel C, Wierczeiko A, Miedema J, Friedrich J, Hofmann F, Weißbach S, Dietrich V, Holthöfer L, Haug V, Mündnich S et al. 2025. Direct RNA sequencing enables improved transcriptome assessment and tracking of RNA modifications for medical applications. *Nucleic Acids Research* **53**.

Huang da W, Sherman BT, Lempicki RA. 2009. Systematic and integrative analysis of large gene lists using DAVID bioinformatics resources. *Nat Protoc* **4**: 44-57.

Jain M, Olsen HE, Paten B, Akeson M. 2016. The Oxford Nanopore MinION: delivery of nanopore sequencing to the genomics community. *Genome Biology* **17**: 239.

Köster J, Rahmann S. 2012. Snakemake--a scalable bioinformatics workflow engine. *Bioinformatics* **28**: 2520-2522.

Li H, Handsaker B, Wysoker A, Fennell T, Ruan J, Homer N, Marth G, Abecasis G, Durbin R. 2009. The Sequence Alignment/Map format and SAMtools. *Bioinformatics* **25**: 2078-2079.

Linder B, Grozhik AV, Olarerin-George AO, Meydan C, Mason CE, Jaffrey SR. 2015. Single-nucleotide-resolution mapping of m6A and m6Am throughout the transcriptome. *Nature Methods* **12**: 767-772.

Liu C, Sun H, Yi Y, Shen W, Li K, Xiao Y, Li F, Li Y, Hou Y, Lu B et al. 2023. Absolute quantification of single-base m(6)A methylation in the mammalian transcriptome using GLORI. *Nat Biotechnol* **41**: 355-366.

Liu JF, Hawley BR, Nicholson LS, Jaffrey SR. 2025. Decoding m(6)Am by simultaneous transcription-start mapping and methylation quantification. *Elife* **13**.

Meyer KD. 2019. DART-seq: an antibody-free method for global m6A detection. *Nature Methods* **16**: 1275-1280.

Meyer Kate D, Saletore Y, Zumbo P, Elemento O, Mason Christopher E, Jaffrey Samie R. 2012. Comprehensive Analysis of mRNA Methylation Reveals Enrichment in 3' UTRs and near Stop Codons. *Cell* **149**: 1635-1646.

Moshitch-Moshkovitz S, Sevilla-Sharon M, Ashwal-Fluss R, Glick-Saar E, Rechavi G, Dominissini D. 2024. mRNA m6A detection. *Nature Reviews Methods Primers* **4**.

Mudge JM, Carbonell-Sala S, Diekhans M, Martinez JG, Hunt T, Jungreis I, Loveland JE, Arnan C, Barnes I, Bennett R et al. 2025. GENCODE 2025: reference gene annotation for human and mouse. *Nucleic Acids Res* **53**: D966-d975.

Murakami S, Jaffrey SR. 2022. Hidden codes in mRNA: Control of gene expression by m(6)A. *Mol Cell* **82**: 2236-2251.

Raymon HK, Thode S, Zhou J, Friedman GC, Pardinas JR, Barrere C, Johnson RM, Sah DWY. 1999. Immortalized Human Dorsal Root Ganglion Cells Differentiate into Neurons with Nociceptive Properties. *The Journal of Neuroscience* **19**: 5420-5428.

Sendinc E, Shi Y. 2023. RNA m6A methylation across the transcriptome. *Mol Cell* **83**: 428-441.

Shen W, Sun H, Liu C, Yi Y, Hou Y, Xiao Y, Hu Y, Lu B, Peng J, Wang J et al. 2024. GLORI for absolute quantification of transcriptome-wide m6A at single-base resolution. *Nature Protocols* **19**: 1252-1287.

Su C-H, D D, Tarn W-Y. 2018. Alternative Splicing in Neurogenesis and Brain Development. *Frontiers in Molecular Biosciences* **Volume 5 - 2018**.

Sun H, Li K, Liu C, Yi C. 2023. Regulation and functions of non-m(6)A mRNA modifications. *Nat Rev Mol Cell Biol* **24**: 714-731.

Sun H, Lu B, Zhang Z, Xiao Y, Zhou Z, Xi L, Li Z, Jiang Z, Zhang J, Wang M et al. 2025. Mild and ultrafast GLORI enables absolute quantification of m6A methylome from low-input samples. *Nature Methods* **22**: 1226-1236.

Verstraten R, Cetraro P, Fitzpatrick AH, Alwie Y, Frommeyer YN, Loliashvili E, Stein SC, Häussler S, Ouwendijk WJD, Depledge DP. 2025. Defining expansions and perturbations to the RNA polymerase III transcriptome and epitranscriptome by modified direct RNA nanopore sequencing. *bioRxiv* doi:10.1101/2025.03.07.641986.

Viehweger A, Krautwurst S, Lamkiewicz K, Madhugiri R, Ziebuhr J, Hölzer M, Marz M. 2019. Direct RNA nanopore sequencing of full-length coronavirus genomes provides novel insights into structural variants and enables modification analysis. *Genome Res* **29**: 1545-1554.

Xiao YL, Liu S, Ge R, Wu Y, He C, Chen M, Tang W. 2023. Transcriptome-wide profiling and quantification of N(6)-methyladenosine by enzyme-assisted adenosine deamination. *Nat Biotechnol* **41**: 993-1003.

Xie YY, Zhong ZD, Chen HX, Ren ZH, Qiu YT, Lan YL, Wu F, Kong JW, Luo RJ, Zhang D et al. 2025. Single-molecule direct RNA sequencing reveals the shaping of epitranscriptome across multiple species. *Nat Commun* **16**: 5119.

602 Xu H, Kong L, Cheng J, Al Moussawi K, Chen X, Iqbal A, Wing PAC, Harris JM, Tsukuda S, Embarc-
603 Buh A et al. 2024. Absolute quantitative and base-resolution sequencing reveals
604 comprehensive landscape of pseudouridine across the human transcriptome. *Nature*
605 *Methods* **21**: 2024-2033.
606 Yang L, Tang L, Min Q, Tian H, Li L, Zhao Y, Wu X, Li M, Du F, Chen Y et al. 2024a. Emerging role of
607 RNA modification and long noncoding RNA interaction in cancer. *Cancer Gene Ther* **31**:
608 816-830.
609 Yang Y, Lu Y, Wang Y, Wen X, Qi C, Piao W, Jin H. 2024b. Current progress in strategies to profile
610 transcriptomic m(6)A modifications. *Front Cell Dev Biol* **12**: 1392159.
611 Yankova E, Blackaby W, Albertella M, Rak J, De Braekeleer E, Tsagkogeorga G, Pilka ES, Aspris D,
612 Leggate D, Hendrick AG et al. 2021. Small-molecule inhibition of METTL3 as a strategy
613 against myeloid leukaemia. *Nature* **593**: 597-601.
614 Yu J, She Y, Ji S-J. 2021. m6A Modification in Mammalian Nervous System Development, Functions,
615 Disorders, and Injuries. *Frontiers in Cell and Developmental Biology* **Volume 9 - 2021**.
616 Zaccara S, Ries RJ, Jaffrey SR. 2019. Reading, writing and erasing mRNA methylation. *Nature*
617 *Reviews Molecular Cell Biology* **20**: 608-624.
618 Zou Y, Ahsan MU, Chan J, Meng W, Gao S-J, Huang Y, Wang K. 2025. A comparative evaluation of
619 computational models for RNA modification detection using nanopore sequencing with
620 RNA004 chemistry. *Briefings in Bioinformatics* **26**.

621

622

623 **Figure legends**

624

625 **Figure 1. Workflow for m^{6}A mapping in different human cell types using orthogonal sequencing**
626 **approaches.**

627 **(A)** Schematic of the experimental setup. RNA was isolated from NHDFs and differentiated HD10.6 cells
628 treated with STM2457 or DMSO for 48h. Poly(A) RNA was subjected to DRS and GLORI from the same
629 input material. IVT RNA was generated in parallel to assess potential false-positive modification calls. **(B)**
630 Workflow for benchmarking Dorado basecalling. Reads were processed with Dorado versions v.0.5.0
631 through v0.9.0, aligned to the human genome or transcriptome, and analyzed with ONT's Modkit tool.
632 Multiple filtering strategies were tested against IVT controls and METTL3 inhibition (STM2457). Resulting
633 m^{6}A sites were compared with GLORI data from the same input RNA. **(C)** Final benchmarked Dorado
634 pipeline to detect high confidence m^{6}A sites.

635

636 **Figure 2. Modification probability of 0.98 and stoichiometry score of ≥ 10% are necessary cutoffs to**
637 **identify m^6A sites accurately.**

638 **(A)** Dorado v0.9.0-generated modification probability distributions for all-context m^6A from genome-
639 aligned DMSO- and STM2457-treated NHDFs plotted against the ones from IVT NHDF poly(A) RNA. DMSO
640 probability score distribution is shown as a red solid line, STM2457 – red dashed line, IVT – grey solid line.
641 **(B)** Same as in (A), but for DRACH-context m^6A sites. **(C)** Stoichiometry (≥ 10%) distributions for all-context
642 m^6A from DMSO- (in red) or STM2457-treated (in pink) NHDF datasets (genome-aligned) are plotted using
643 a 0.98 modification probability cutoff and a filter for ≥ 20 reads. **(D)** Same as in (C), but for DRACH-context
644 m^6A sites. **(E)** Overlap of m^6A sites between all-context and DRACH models (A basecall accuracy ≥ 80%,
645 coverage ≥ 20reads, stoichiometry ≥ 10%), comparing non-filtered to filtered (modification probability >
646 0.98) outputs. **(F)** Metagene plots showing the density of m^6A (all-context – dark red, DRACH-context –
647 bright red) sites across all annotated poly(A) transcripts (left) and monoexonic poly(A) transcripts (right)
648 from genome-aligned DMSO-treated NHDF datasets filtered with 0.98 modification probability, ≥ 20
649 coverage and ≥ 10% stoichiometry.

650

651 **Figure 3. Comparison of m^6A sites detected by Dorado and GLORI.**

652 **(A)** Filtering strategy for Dorado vs GLORI to obtain a high-confidence list of m^6A sites in NHDFs. **(B)**
653 Stoichiometry distributions are plotted from genome-aligned DMSO- or STM2457-treated NHDF datasets
654 using the indicated Dorado models and the filtering strategy shown in (A). **(C)** Stoichiometry distributions
655 from GLORI performed on DMSO- or STM2457-treated NHDFs are plotted, using the filtering strategy
656 shown in (A). In addition, m^6A sites were filtered for DRACH motifs (right plot). **(D)** Overlap of high
657 confidence m^6A sites detected by Dorado vs GLORI. GLORI datasets were filtered using increasing m^6A
658 stoichiometry cutoffs (from left to right). **(E)** m^6A sites in the *SPEN* gene detected by GLORI and Dorado.
659 Boxplots (right) represent the m^6A stoichiometries per m^6A site shown on the left. **(F)** *SPEN* isoforms with
660 m^6A sites, determined by Dorado. Boxplots (right) show the distribution of m^6A stoichiometries on the
661 m^6A sites on *SPEN-201* and *SPEN-202*.

662

663 **Figure 4. Comparative analysis of m^6A modification patterns in NHDFs and HD10.6 cells using Dorado**
664 **v0.9.0.**

(A) Overlap of high confidence m^6A sites between NHDFs and HD10.6 cells. **(B)** Correlation of shared m^6A stoichiometries (n=38,217). **(C)** Boxplots showing the m^6A stoichiometry distributions of the 38,217 detected in both NHDFs and HD10.6 cells. **(D+E)** Motif analysis showing m^6A (all-context and DRACH-context) motif logos, 5-mer distributions and modification stoichiometries in NHDFs. **(F+G)** Same as in (D+E) but for HD10.6 cells. **(H)** KEGG pathway analysis (DAVID Bioinformatics Resources) of shared m^6A-containing genes. **(I)** m^6A stoichiometries of representative examples of individual genes from enriched pathways (H). *ACTG1* serves as a housekeeping control.

Figure S1. Evaluation of Dorado by base and modification probability distributions.

(A) Dorado v0.9.0-generated basecall accuracy probability values for A (all-context and DRACH-context basecaller models) from genome-aligned DMSO- and STM2457-treated NHDF samples against IVT poly(A) NHDF RNA. A probability score distribution is shown as a black solid line for DMSO, STM2457 – black dashed line, IVT – grey solid line. **(B)** Dorado v0.9.0-generated modification probability distributions, visualized as histograms, for DRACH-context m^6A from genome-aligned DMSO- and STM2457-treated NHDFs and IVT NHDFs. IVT modification probability score distribution is shown in grey, DMSO – bright red, STM2457 – dark red. **(C)** Same as in (B), but for all-context m^6A sites.

Figure S2. Modification probability cutoffs are necessary to identify Ψ and inosine sites more accurately.

(A) Dorado v0.9.0-generated basecall accuracy probability values for U (left) and modification probability distributions for Ψ (right) from genome-aligned DMSO- and STM2457-treated NHDF samples are plotted against IVT poly(A) RNA. Ψ probabilities are visualized in blue solid and dashed lines for DMSO and STM2457, respectively and in grey solid line for IVT. **(B)** Same as in (A) but showing A base accuracy probabilities and inosine sites. Inosine probabilities are visualized in purple solid and dashed lines for DMSO and STM2457, respectively and in grey solid line for IVT. **(C)** Same as in (A) but showing C base accuracy probabilities and m^5C sites. m^5C probabilities are visualized in green solid and dashed lines for DMSO and STM2457, respectively and in grey solid line for IVT. **(D+E)** DRACH-context and all-context m^6A modification probability distributions (red) from genome-aligned DMSO- and STM2457-treated NHDFs are plotted against RCS negative control (grey).

694 **Figure S3. Modification probability cutoffs are necessary to identify modification sites accurately, shown**
695 **for transcriptome-aligned data.**

696 Dorado v0.9.0-generated basecall accuracy probability values for A, U and C (left, **A-E**) and modification
697 probability distributions for m^6A (all-context), m^6A (DRACH-context), Ψ, inosine and m^5C (right, **A-E**) in
698 transcriptome-aligned DMSO-and STM2457-treated NHDFs, plotted against the values from IVT NHDF
699 poly(A) RNA.

700

701 **Figure S4. Modification probability distribution profiles in genome-aligned DMSO-and STM2457-treated**
702 **HD10.6 cells.**

703 Dorado v0.9.0-generated basecall accuracy probability values for A, U and C (left, **A-E**) and modification
704 probability distributions for m^6A (all-context), m^6A (DRACH-context), Ψ, inosine and m^5C (right, **A-E**) in
705 human genome-aligned DMSO-and STM2457-treated HD10.6 cells, plotted against the values from IVT
706 NHDF poly(A) RNA.

707

708 **Figure S5. Modification probability distribution profiles in transcriptome-aligned DMSO-and STM2457-**
709 **treated HD10.6 cells.**

710 Dorado v0.9.0-generated basecall accuracy probability values for A, U and C (left, **A-E**) and modification
711 probability distributions for m^6A (all-context), m^6A (DRACH-context), Ψ, inosine and m^5C (right, **A-E**) in
712 human transcriptome-aligned DMSO-and STM2457-treated HD10.6 cells, plotted against the values from
713 IVT NHDF poly(A) RNA.

714

715 **Figure S6. Modification site probabilities detected with different versions of Dorado and compared to**
716 **RCS.**

717 **(A+B)** DRACH-context and all-context m^6A modification probability distributions from genome-aligned
718 DMSO (solid red line)- and STM2457 (dashed red line)-treated NHDFs are plotted against RCS negative
719 control (grey). **(C)** Modification probability distributions for all-context m^6A (Dorado v0.7.0, v0.8.0 and
720 v0.9.0), the bottom panel showing the distributions in 0.95-1.00 modification range. **(D)** Same as in (C),
721 but for DRACH-context m^6A (Dorado v0.5.0, v0.6.0, v0.8.0 and v0.9.0). **(E)** Same as in (C), but for Ψ (Dorado

722 v0.7.0, v0.8.0, v0.9.0). All the plots in C-E are generated from genome-aligned DMSO-treated NHDF
723 datasets and are plotted against RCS negative controls.

724

725 **Figure S7. Evaluation of Dorado by stoichiometry distributions.**

726 **(A)** Stoichiometry distributions for all-context m^6A from DMSO- (in red) or STM2457-treated (in pink) NHDF
727 datasets (genome-aligned and filtered for ≥ 20 reads) are plotted, comparing 0.98 modification probability-
728 unfiltered (left) and filtered (right) sites. **(B)** Same as in (A), but for DRACH-context m^6A sites.

729

730 **Figure S8. Stoichiometry distributions of m^6A, Ψ and inosine in IVT datasets.**

731 **(A)** All-context m^6A stoichiometry distributions (all stoichiometries (top) and ≥ 10% stoichiometries
732 (bottom)) in (genome-aligned) IVT RNA from DMSO-treated NHDFs, comparing modification probability-
733 unfiltered and filtered data. The bottom panel shows stoichiometry distributions only for ≥ 10%
734 stoichiometry sites. **(B)** As in (A), but for DRACH-context m^6A. **(C)** As in (A), but for Ψ. **(D)** As in (A), but for
735 inosine.

736

737 **Figure S9. Evaluation of Dorado by stoichiometry distributions in transcriptome-aligned NHDFs.**

738 **(A)** Stoichiometry distributions for all-context m^6A from DMSO- (in red) or STM2457-treated (in pink) NHDF
739 datasets (transcriptome-aligned and filtered for ≥ 20 reads) are plotted, assessing the 0.98 modification
740 probability cutoff. The bottom panel shows stoichiometry distributions only for ≥ 10% stoichiometry sites.
741 **(B)** Same as in (A), but for DRACH-context m^6A sites.

742

743 **Figure S10. Evaluation of Dorado by stoichiometry distributions in transcriptome-aligned HD10.6 cells.**

744 **(A)** Stoichiometry distributions for all-context m^6A from DMSO- (in red) or STM2457-treated (in pink)
745 HD10.6 datasets (transcriptome-aligned and filtered for ≥ 20 reads) are plotted, assessing the 0.98
746 modification probability cutoff. The bottom panel shows stoichiometry distributions only for ≥ 10%
747 stoichiometry sites. **(B)** Same as in (A), but for DRACH-context m^6A sites.

748

Figure S11 Stoichiometry distributions of Ψ and inosine in NHDFs.

(A) Distributions of all (left) and ≥ 10% (right) Ψ stoichiometries in the 0.99 modification probability-unfiltered and filtered data from genome-aligned DMSO- (darker color) and STM2457-treated (lighter color) NHDFs (filtered for ≥ 20 reads). **(B)** Same as in (A), but for inosine.

Figure S12. Stoichiometry distributions of Ψ and inosine in HD10.6 cells.

(A) Distributions of all and ≥ 10% Ψ stoichiometries in the 0.99 modification probability-unfiltered and filtered data from genome-aligned DMSO- (darker color) and STM2457-treated (lighter color) HD10.6 cells (filtered for ≥ 20 reads). **(B)** Same as in (A), but for inosine.

Figure S13. m^6A and Ψ stoichiometry distributions in different versions of Dorado.

Stoichiometry distributions (all stoichiometries – left, ≥ 10% stoichiometries – right) in a line graph format for **(A)** all-context m^6A detected in genome-aligned DMSO-treated NHDF dataset, with Dorado versions 0.7.0, 0.8.0 and 0.9.0 colored in gradients of red, darkness increasing with the later versions. **(B)** DRACH-context m^6A detected with Dorado versions 0.5.0, 0.6.0, 0.8.0 and 0.9.0, colored in gradients of red, darkness increasing with the later versions. **(C)** Ψ detected with Dorado versions 0.7.0, 0.8.0 and 0.9.0, colored in gradients of blue, darkness increasing with the later versions. All the datasets were filtered for ≥ 20 reads.

Figure S14. Comparison of modification sites detected with different versions of Dorado.

Upset plots showing unique and shared detected modifications (filtered for ≥ 20 reads, ≥ 10% stoichiometry) in modification probability-unfiltered and filtered genome-aligned DMSO-treated NHDF data. The versions are ordered on the plot by the number of detected sites, in ascending order (on the left). Results are shown for the following models and versions: **(A)** all-context m^6A detected with v.0.7.0, v0.8.0 and v0.9.0, **(B)** DRACH-context m^6A detected with v.0.5.0, v0.6.0, v0.8.0 and v0.9.0, **(C)** Ψ detected with v.0.7.0, v0.8.0 and v0.9.0. **(D)** Nucleotide frequencies in the 5-base motif of Ψ sites for uniquely v0.7.0-, v0.8.0-0.9.0- and v0.7.0-0.8.0-0.9.0-detected Ψ sites. Position 0 marks the modification site.

Figure S15. Comparison of m^6A sites detected by Dorado and GLORI-Sequencing in NHDFs and HD10.6s.

(A) Upset plot showing the number of m^6A sites detected by GLORI and Dorado in NHDFs and their overlaps. Dorado sites represent high-confidence m^6A sites obtained after filtering DRACH-model detected data. Similarly, only high confidence m^6A sites detected by GLORI are shown but were additionally filtered for DRACH sites. **(B)** Stoichiometry distributions are plotted from genome-aligned DMSO- or STM2457-treated HD10.6 datasets using the indicated Dorado models. **(C)** Stoichiometry distributions from GLORI performed on DMSO- or STM2457-treated NHDFs are plotted. In addition, m^6A sites were filtered for DRACH motifs (right plot). **(D)** Stoichiometry distributions are plotted from transcriptome-aligned DMSO- or STM2457-treated NHDF datasets using the indicated Dorado models. **(E)** Stoichiometry distributions are plotted from transcriptome-aligned DMSO- or STM2457-treated HD10.6 datasets using the indicated Dorado models.

Figure S16. m^6A (all-context and DRACH-context) motif logos for modification probability-unfiltered NHDF and HD10.6 data.

(A) 5-mer motif logo (showing nucleotide frequences at each position) of m^6A-modified sites (position 0 = modified A) from genome-aligned DMSO-treated NHDFs (all-context – left, DRACH-context – right). All the datasets were filtered for ≥ 20 coverage & ≥ 10% stoichiometry. **(B)** Same as (A), but for HD10.6 cells.

Figure S17. Metagene plots showing m^6A (all-context and DRACH-context) distribution profiles in NHDF and HD10.6 data filtered at different stoichiometries.

(A) Metagene plots showing the density of m^6A (all-context – dark red, DRACH-context – bright red) sites across all annotated poly(A) transcripts (upper plot) and monoexonic poly(A) transcripts (lower plot) from genome-aligned DMSO-treated NHDF datasets filtered with 0.98 modification probability, ≥ 20 coverage and ≥ 10% stoichiometry. **(B)** The density of all-context m^6A sites (0.98 modification probability-unfiltered – left, filtered – right) is plotted across all annotated poly(A) transcripts of NHDF (dark red) and HD10.6 (bright red) datasets, filtered with different stoichiometries (descending: all stoichiometries, ≥ 50%, ≥ 10% and < 10%. All datasets were filtered additionally for ≥ 20 coverage & ≥ 10% stoichiometry. **(C)** Same as (A), but for DRACH-context m^6A sites.

Figure 1

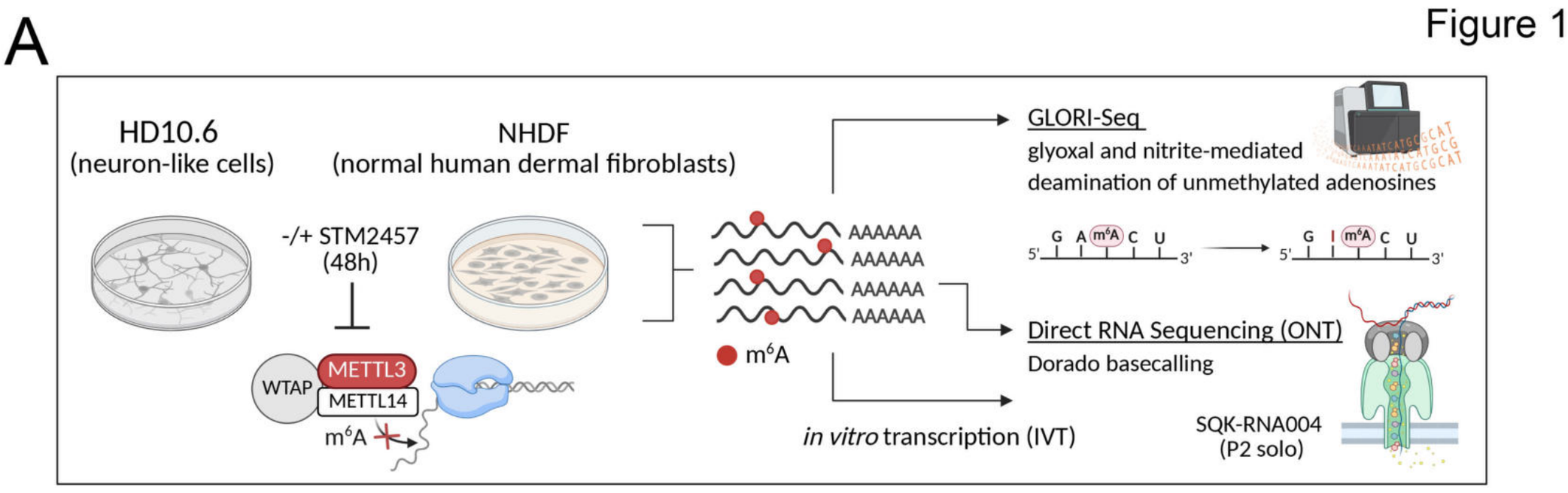
A
HD10.6
(neuron-like cells)
NHDF
(normal human dermal fibroblasts)
-/+ STM2457
(48h)
WTAP
METTL3
METTL14
m6A
AAAAAA
m6A
GLORI-Seq
glyoxal and nitrite-mediated
deamination of unmethylated adenosines
G A m6A C U
G I m6A C U
Direct RNA Sequencing (ONT)
Dorado basecalling
in vitro transcription (IVT)
SQK-RNA004
(P2 solo)

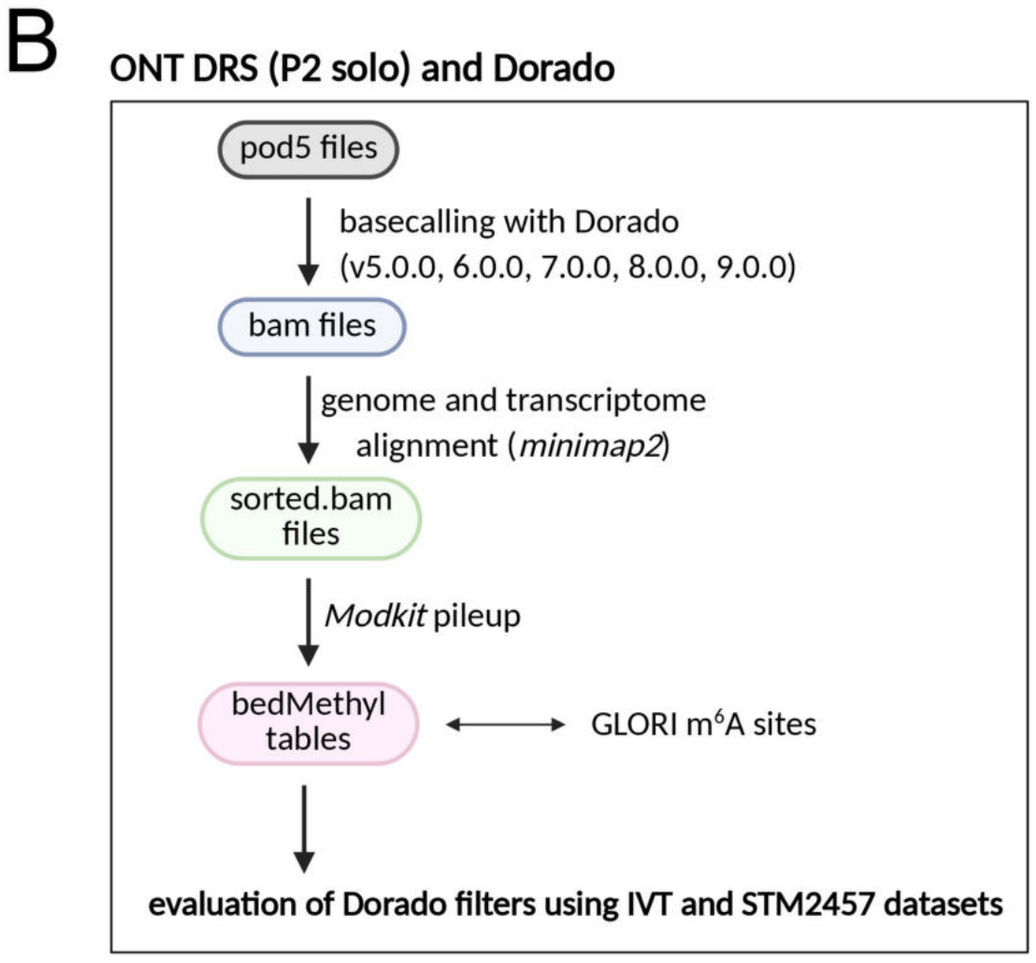
B
ONT DRS (P2 solo) and Dorado
pod5 files
basecalling with Dorado
(v5.0.0, 6.0.0, 7.0.0, 8.0.0, 9.0.0)
bam files
genome and transcriptome
alignment (minimap2)
sorted.bam
files
Modkit pileup
bedMethyl
tables
GLORI m6A sites
evaluation of Dorado filters using IVT and STM2457 datasets

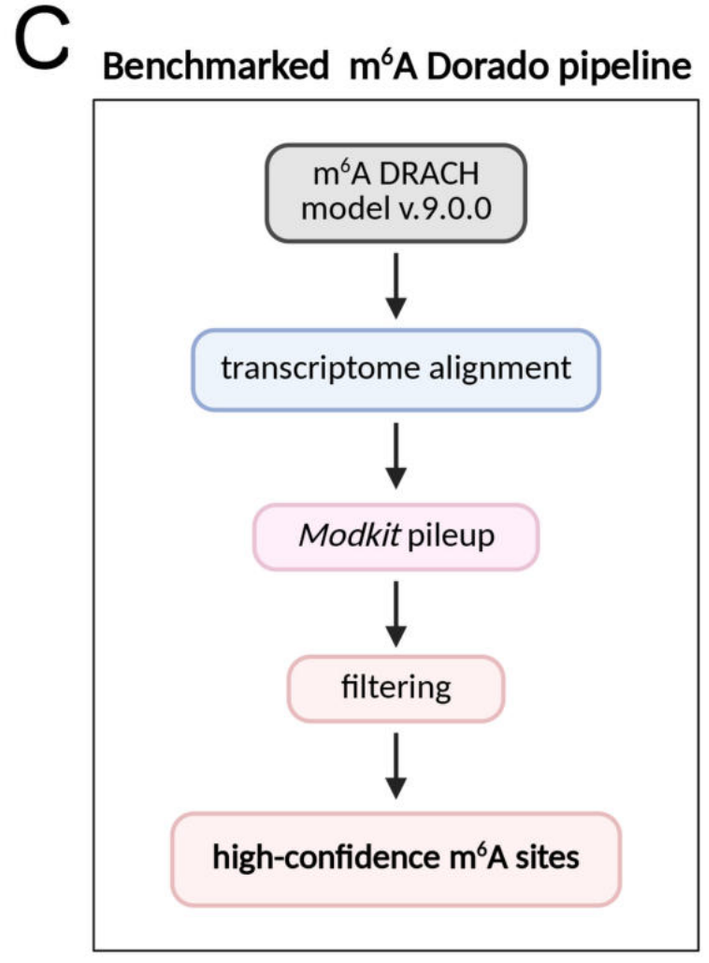
C
Benchmarked m6A Dorado pipeline
m6A DRACH
model v.9.0.0
transcriptome alignment
Modkit pileup
filtering
high-confidence m6A sites

Figure 2

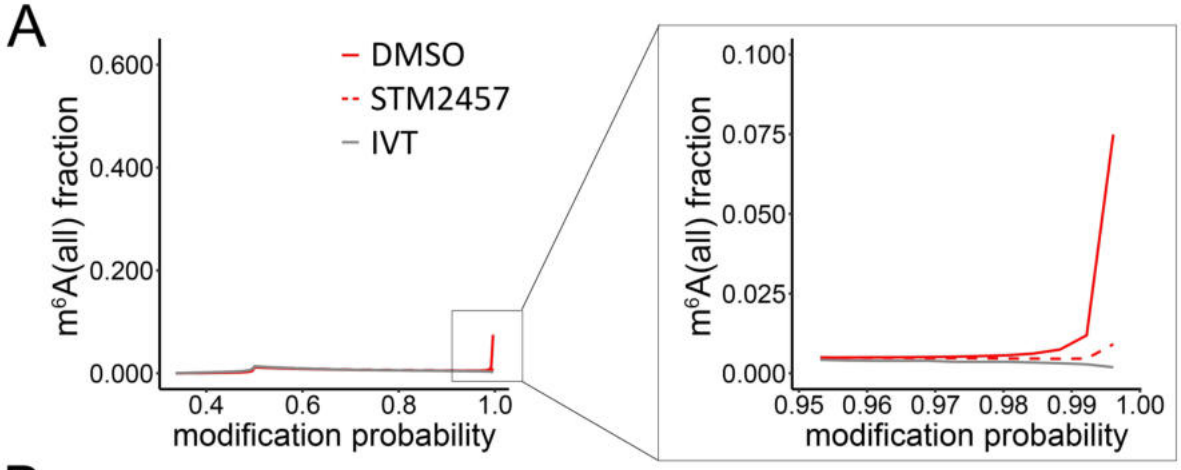
A
DMSO
STM2457
IVT
m6A(all) fraction
modification probability

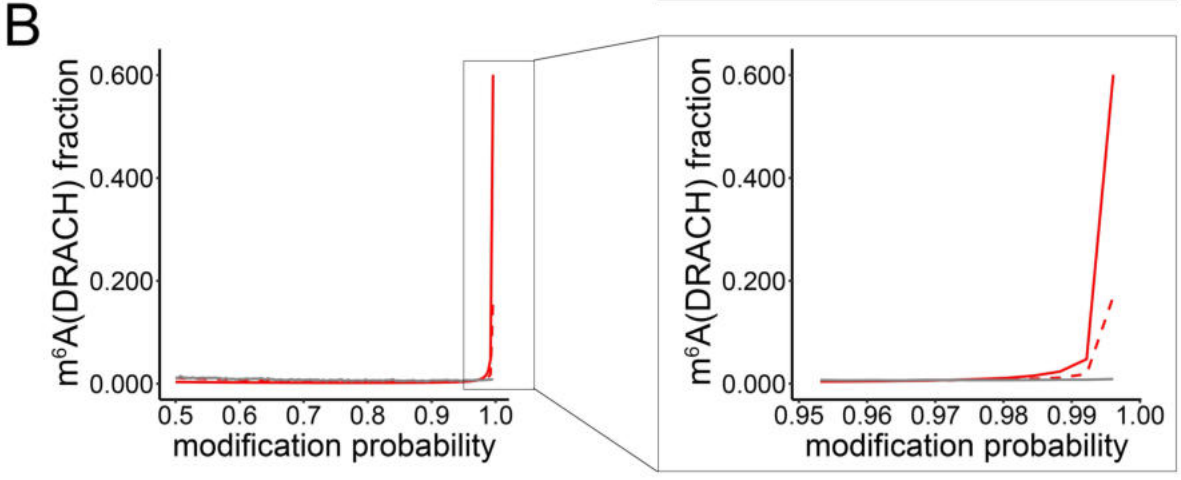
B
m6A(DRACH) fraction
modification probability

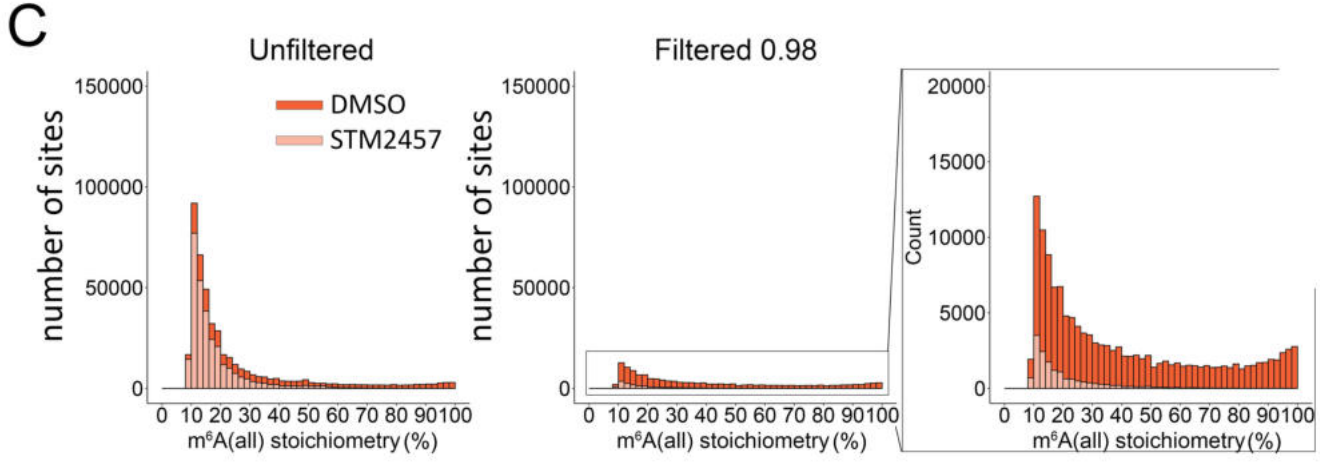
C
Unfiltered
Filtered 0.98
DMSO
STM2457
number of sites
Count
m6A(all) stoichiometry (%)

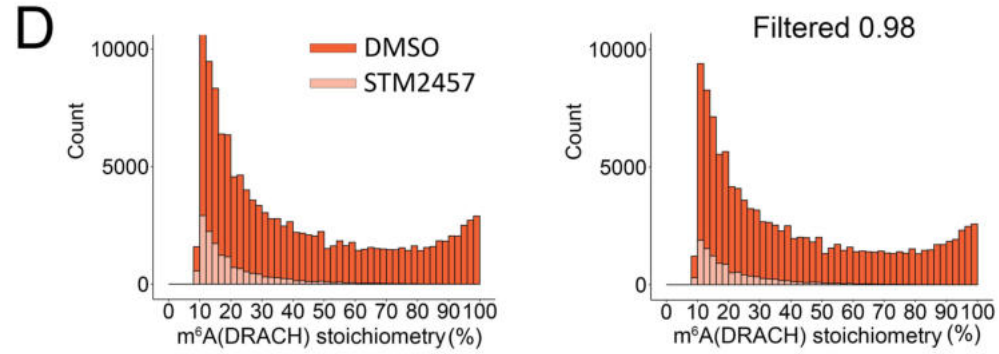
D
DMSO
STM2457
Filtered 0.98
Count
m6A(DRACH) stoichiometry (%)

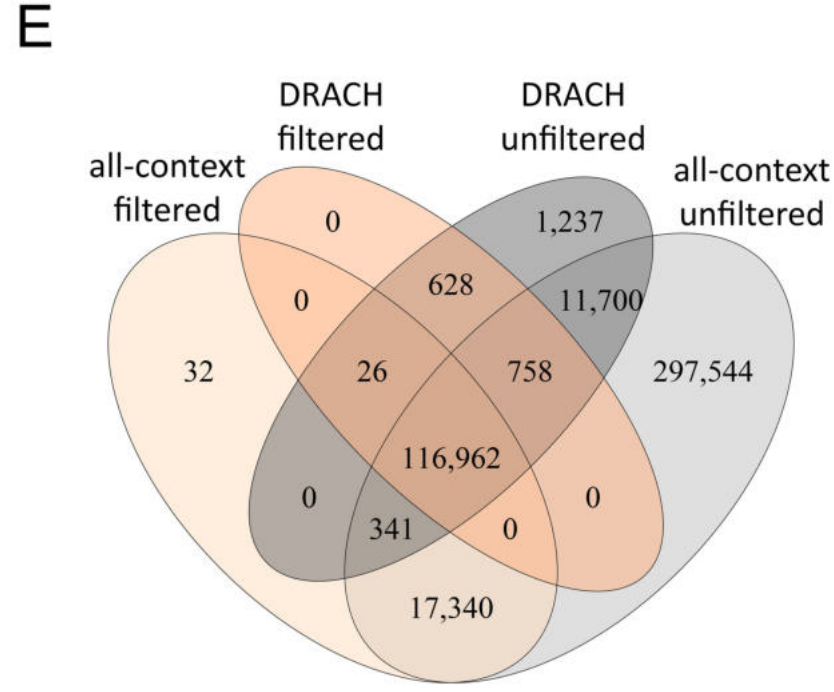
E
all-context filtered
DRACH filtered
DRACH unfiltered
all-context unfiltered
0
1,237
628
11,700
0
32
26
758
297,544
116,962
0
0
341
0
17,340

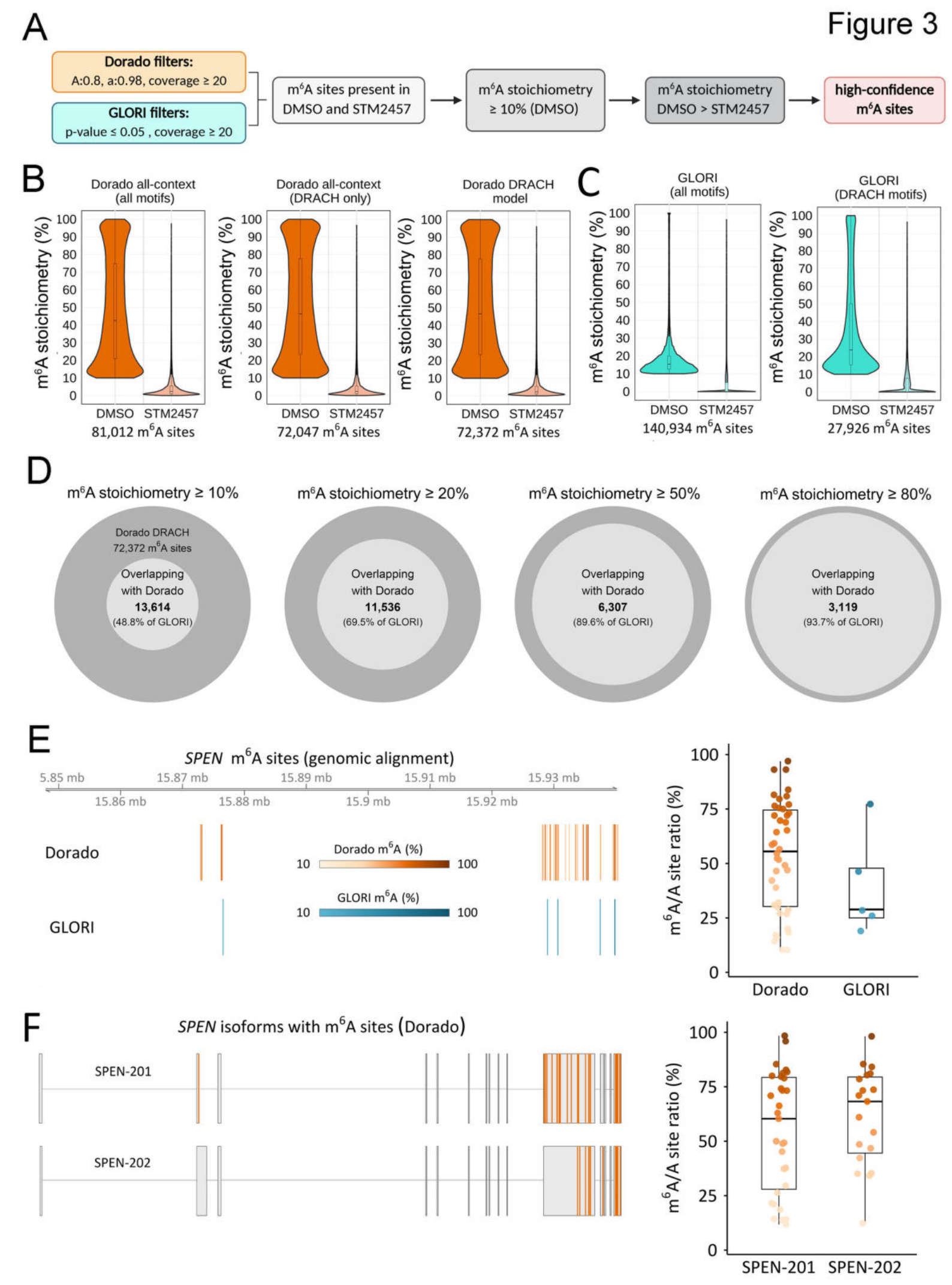
Figure 3
A
Dorado filters:
A:0.8, a:0.98, coverage ≥ 20
GLORI filters:
p-value ≤ 0.05 , coverage ≥ 20
m6A sites present in DMSO and STM2457
m6A stoichiometry ≥ 10% (DMSO)
m6A stoichiometry DMSO > STM2457
high-confidence m6A sites
B
Dorado all-context (all motifs)
Dorado all-context (DRACH only)
Dorado DRACH model
m6A stoichiometry (%)
DMSO STM2457
81,012 m6A sites
72,047 m6A sites
72,372 m6A sites
C
GLORI (all motifs)
GLORI (DRACH motifs)
140,934 m6A sites
27,926 m6A sites
D
m6A stoichiometry ≥ 10%
m6A stoichiometry ≥ 20%
m6A stoichiometry ≥ 50%
m6A stoichiometry ≥ 80%
Dorado DRACH 72,372 m6A sites
Overlapping with Dorado 13,614 (48.8% of GLORI)
Overlapping with Dorado 11,536 (69.5% of GLORI)
Overlapping with Dorado 6,307 (89.6% of GLORI)
Overlapping with Dorado 3,119 (93.7% of GLORI)
E
SPEN m6A sites (genomic alignment)
5.85 mb 15.87 mb 15.89 mb 15.91 mb 15.93 mb
15.86 mb 15.88 mb 15.9 mb 15.92 mb
Dorado
GLORI
Dorado m6A (%)
GLORI m6A (%)
m6A/A site ratio (%)
Dorado GLORI
F
SPEN isoforms with m6A sites (Dorado)
SPEN-201
SPEN-202
m6A/A site ratio (%)
SPEN-201 SPEN-202

Figure 4

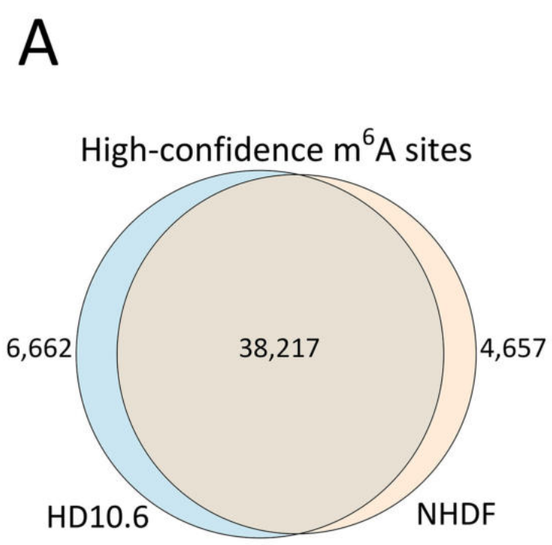
A
High-confidence m6A sites
6,662
38,217
4,657
HD10.6
NHDF

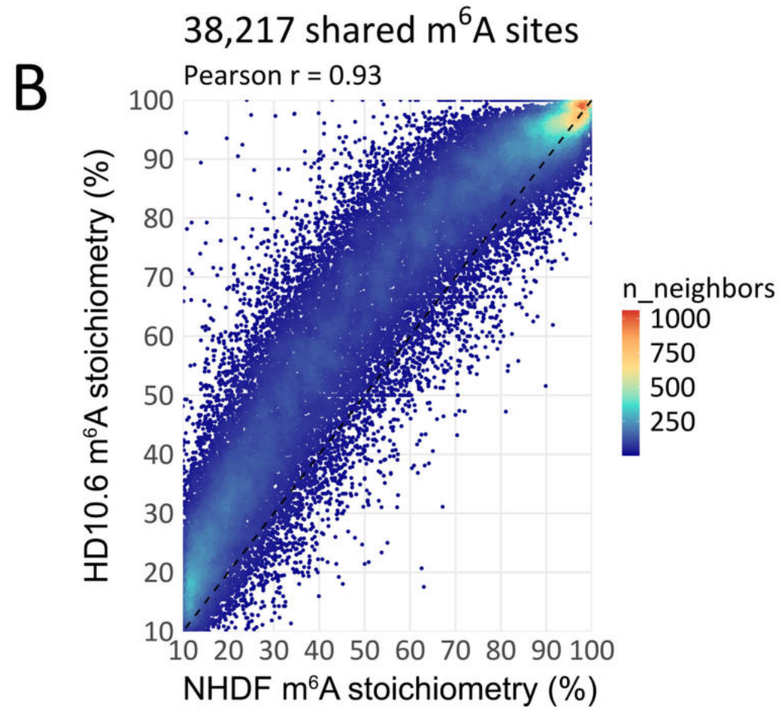
B
38,217 shared m6A sites
Pearson r = 0.93
HD10.6 m6A stoichiometry (%)
NHDF m6A stoichiometry (%)
n_neighbors
1000
750
500
250

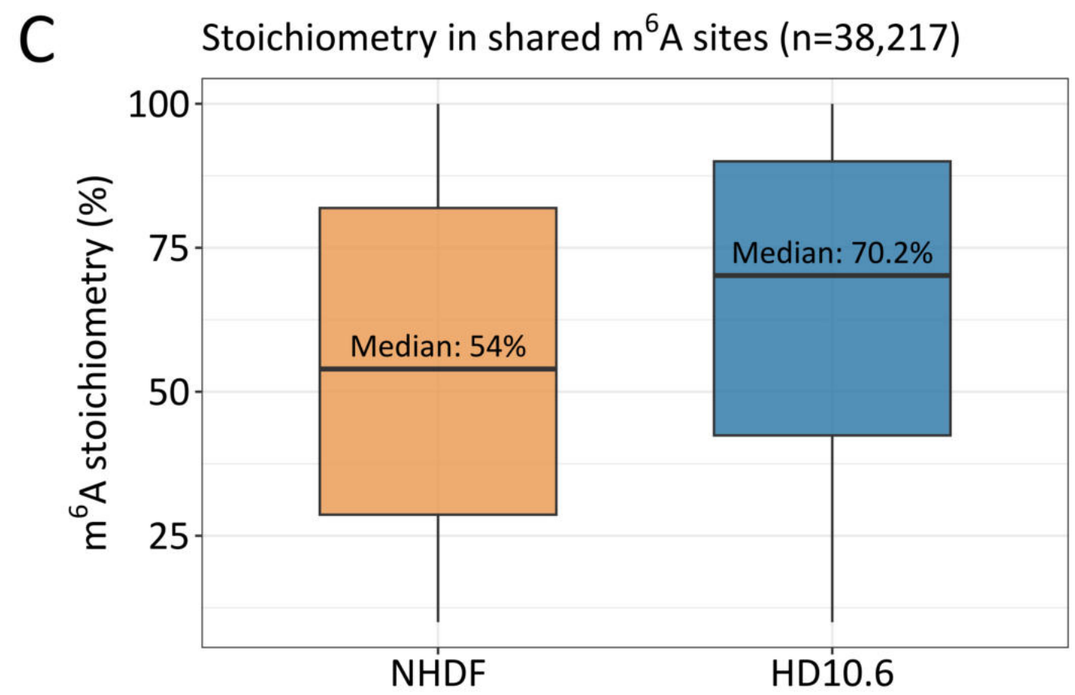
C
Stoichiometry in shared m6A sites (n=38,217)
m6A stoichiometry (%)
Median: 54%
Median: 70.2%
NHDF
HD10.6

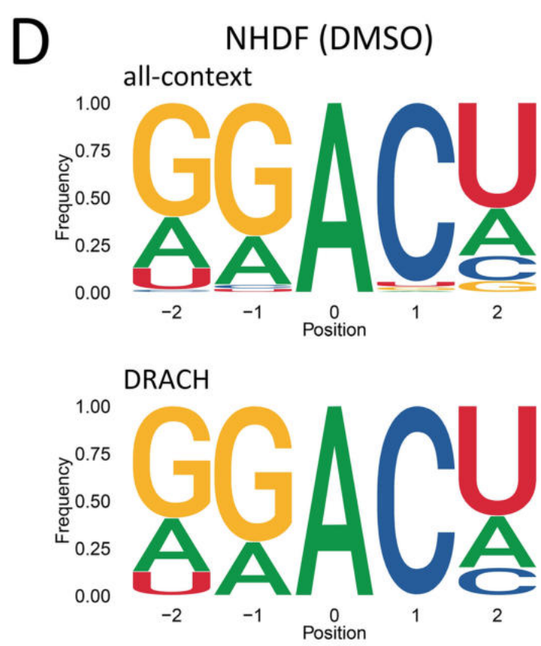
D
NHDF (DMSO)
all-context
DRACH
Frequency
Position

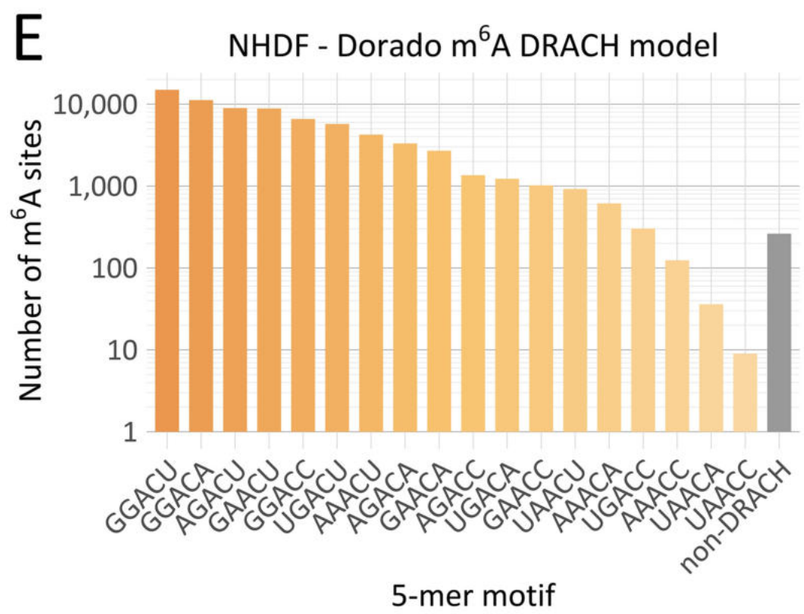
E
NHDF - Dorado m6A DRACH model
Number of m6A sites
5-mer motif

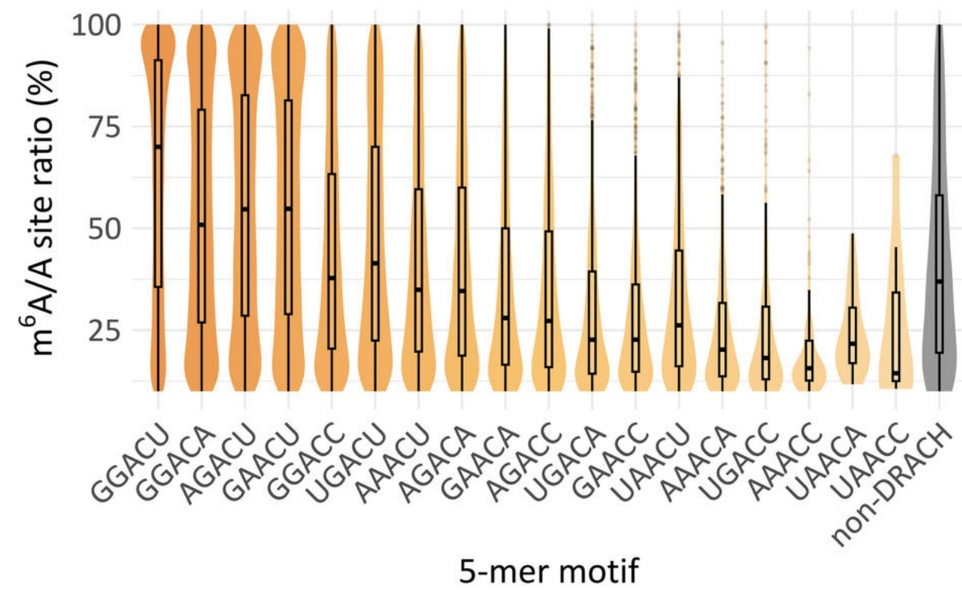
m6A/A site ratio (%)
5-mer motif

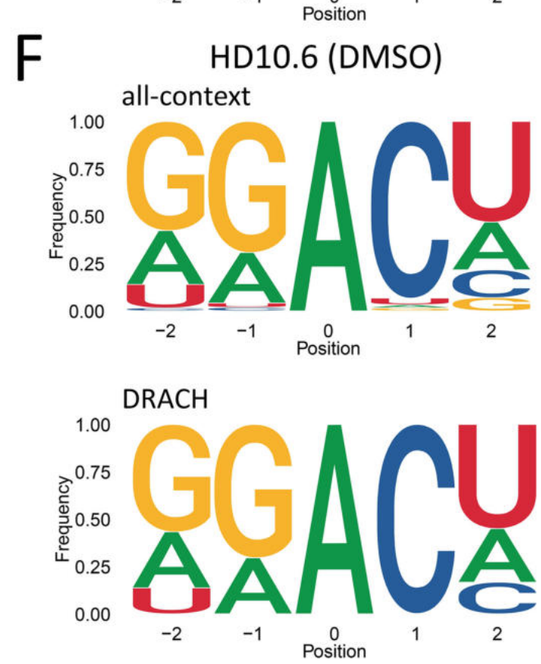
F
HD10.6 (DMSO)
all-context
DRACH
Frequency
Position

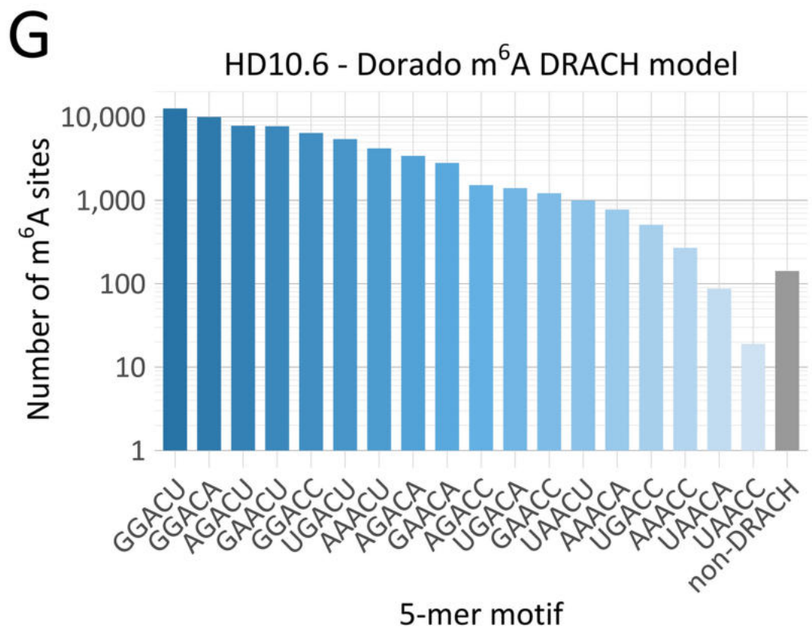
G
HD10.6 - Dorado m6A DRACH model
Number of m6A sites
5-mer motif

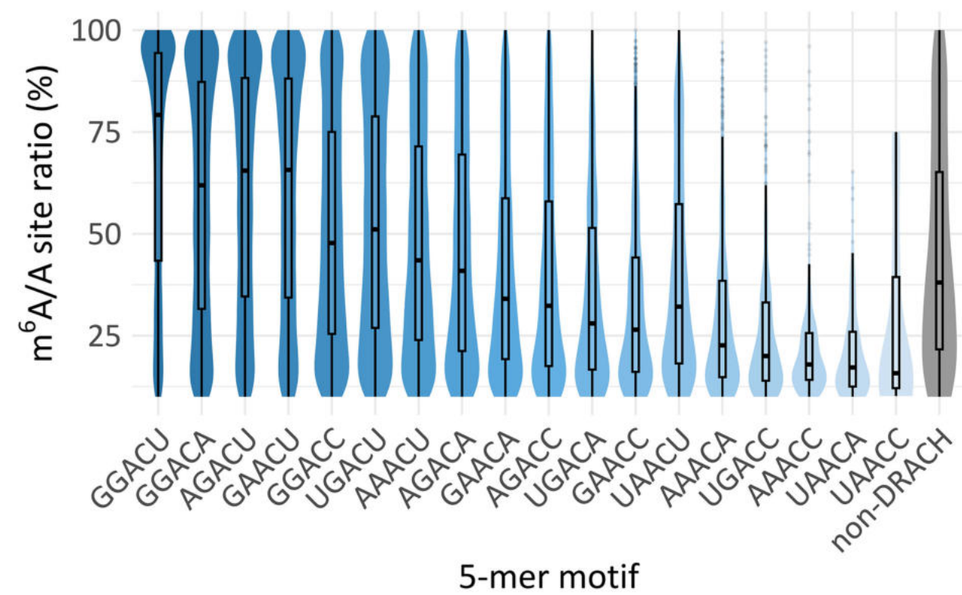
m6A/A site ratio (%)
5-mer motif

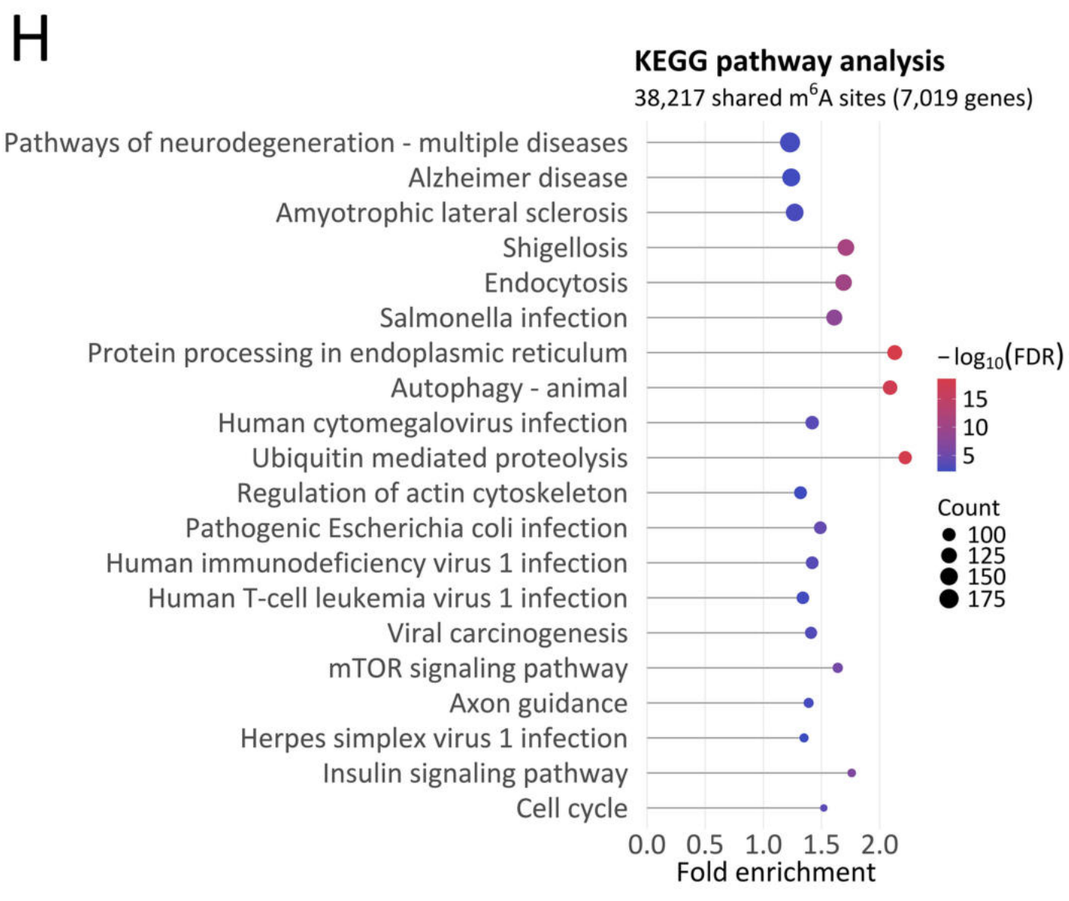
H
KEGG pathway analysis
38,217 shared m6A sites (7,019 genes)
Pathways of neurodegeneration - multiple diseases
Alzheimer disease
Amyotrophic lateral sclerosis
Shigellosis
Endocytosis
Salmonella infection
Protein processing in endoplasmic reticulum
Autophagy - animal
Human cytomegalovirus infection
Ubiquitin mediated proteolysis
Regulation of actin cytoskeleton
Pathogenic Escherichia coli infection
Human immunodeficiency virus 1 infection
Human T-cell leukemia virus 1 infection
Viral carcinogenesis
mTOR signaling pathway
Axon guidance
Herpes simplex virus 1 infection
Insulin signaling pathway
Cell cycle
Fold enrichment
−log10(FDR)
Count

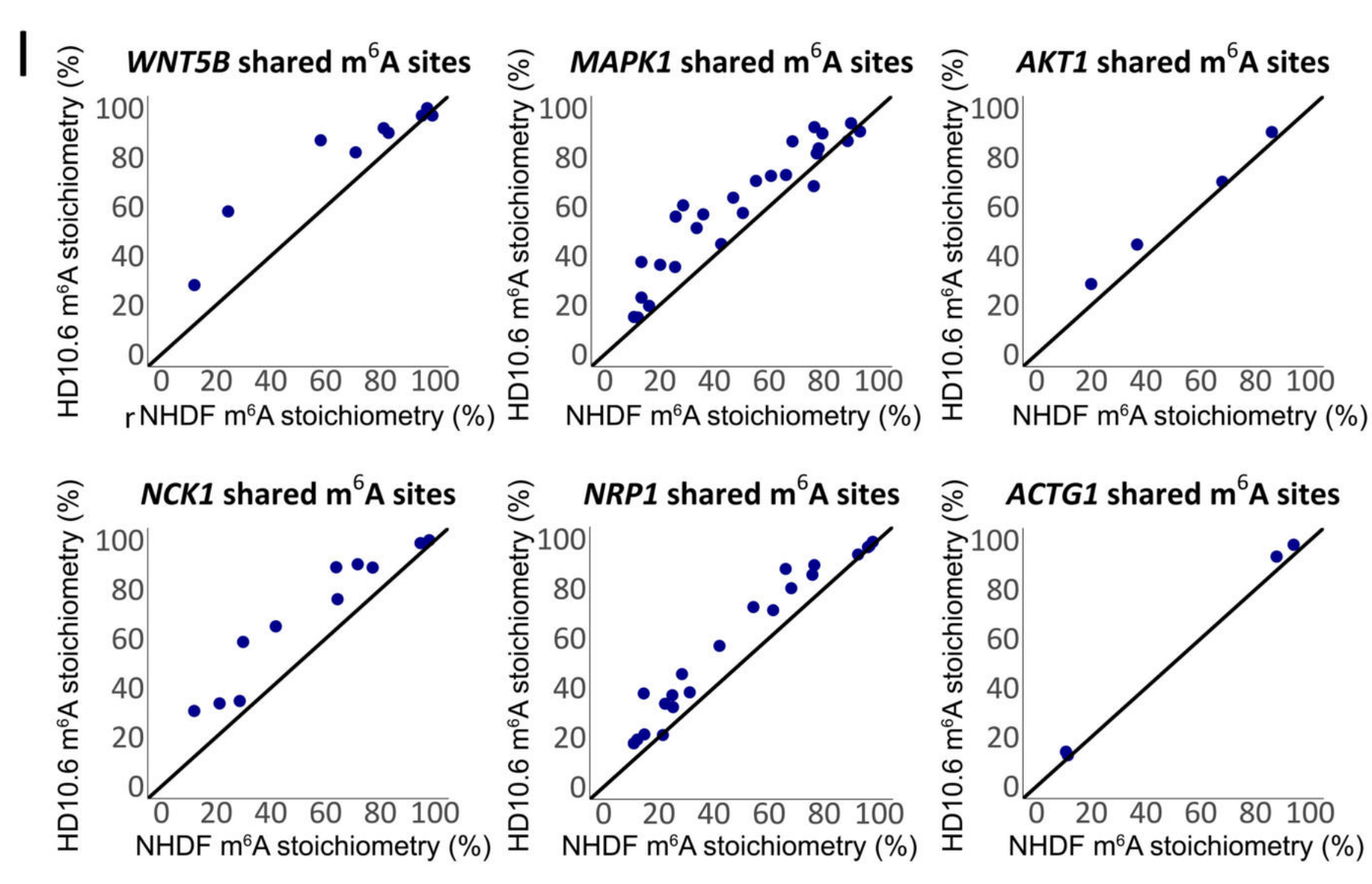
I
WNT5B shared m6A sites
MAPK1 shared m6A sites
AKT1 shared m6A sites
NCK1 shared m6A sites
NRP1 shared m6A sites
ACTG1 shared m6A sites
HD10.6 m6A stoichiometry (%)
NHDF m6A stoichiometry (%)

Figure S1

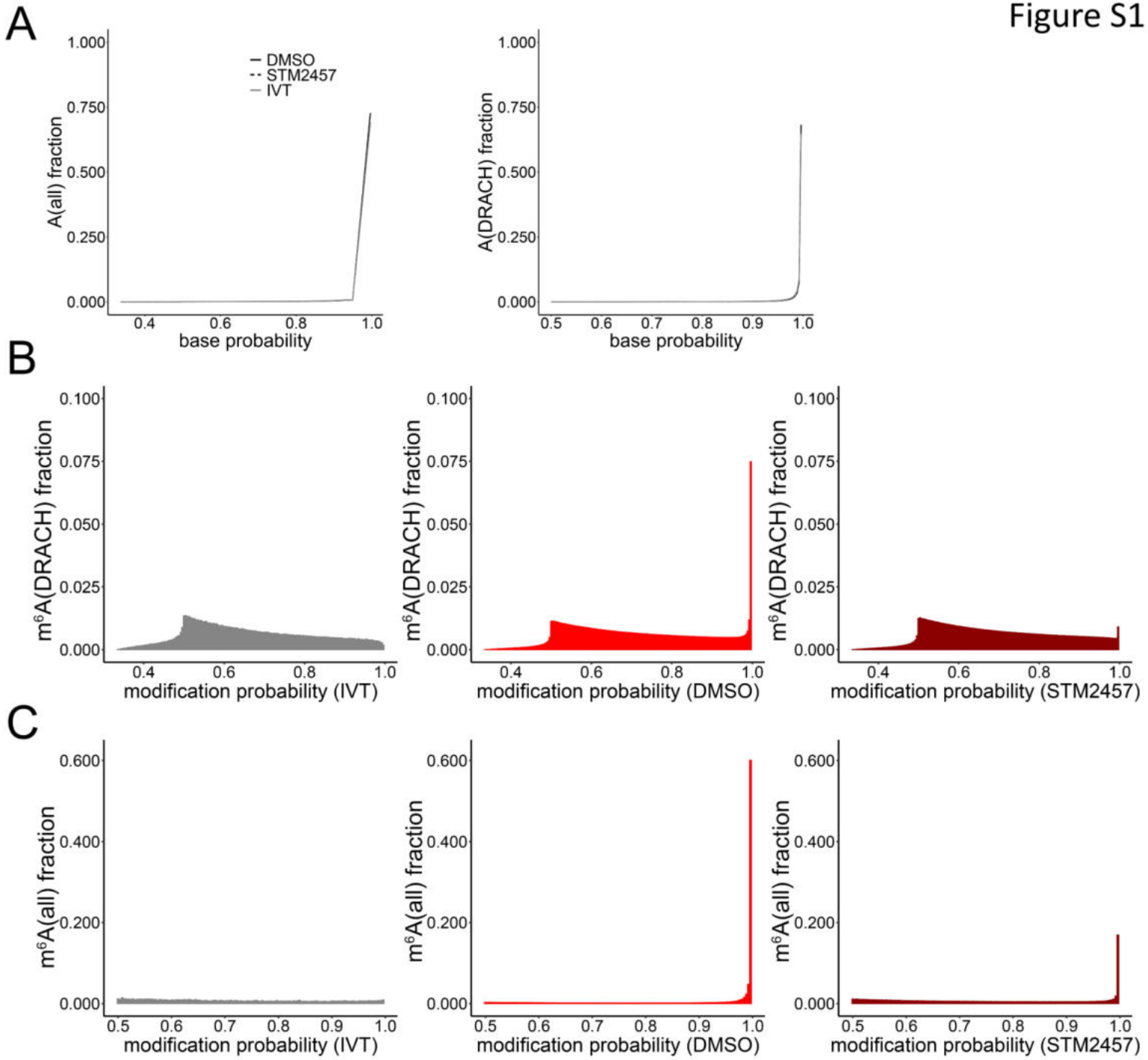
A
DMSO
STM2457
IVT
A(all) fraction
base probability
A(DRACH) fraction
base probability
B
m6A(DRACH) fraction
modification probability (IVT)
modification probability (DMSO)
modification probability (STM2457)
C
m6A(all) fraction
modification probability (IVT)
modification probability (DMSO)
modification probability (STM2457)

Figure S2

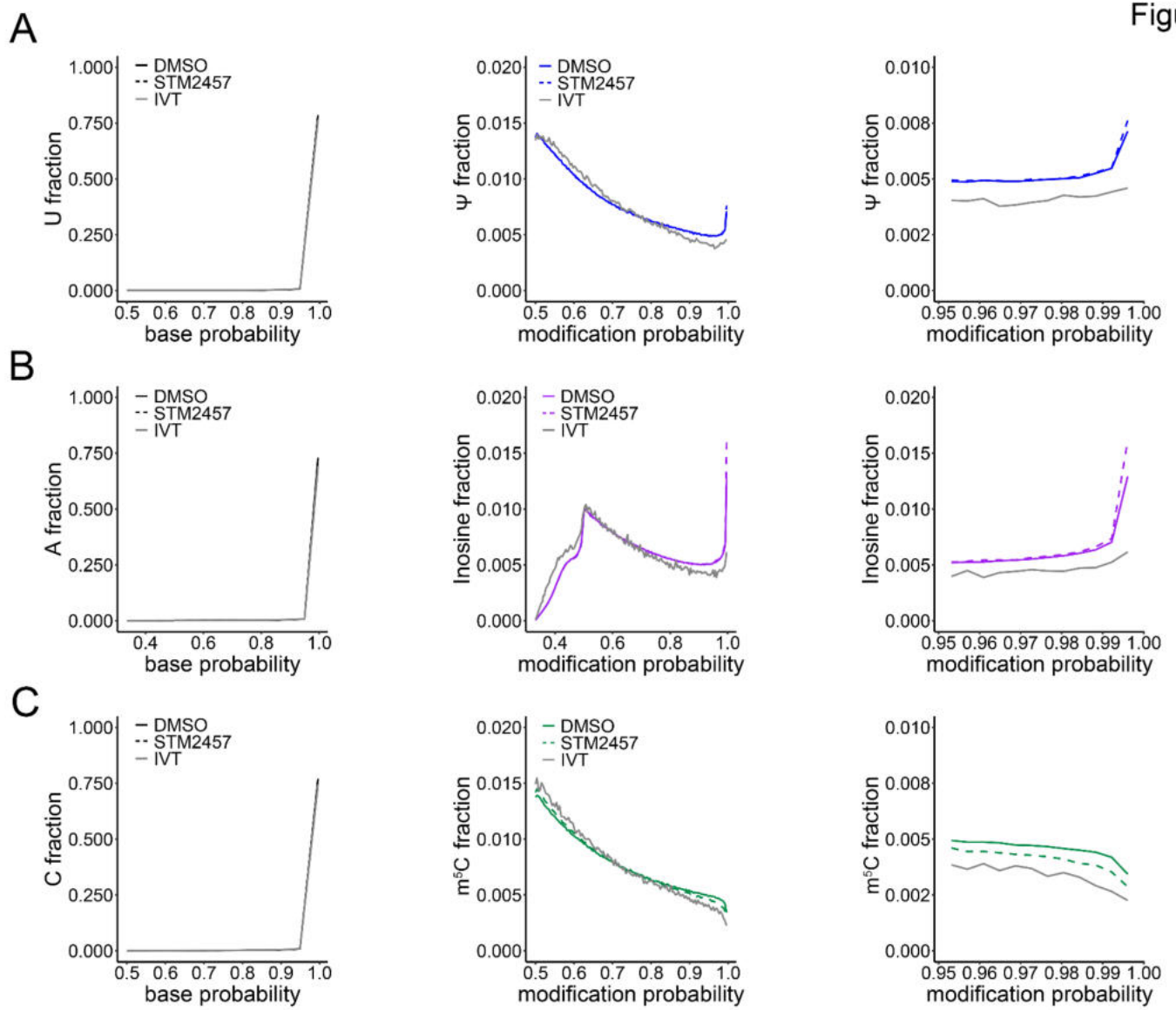
A
DMSO
STM2457
IVT
U fraction
base probability
ψ fraction
modification probability
B
A fraction
Inosine fraction
C
C fraction
m5C fraction

Figure S3

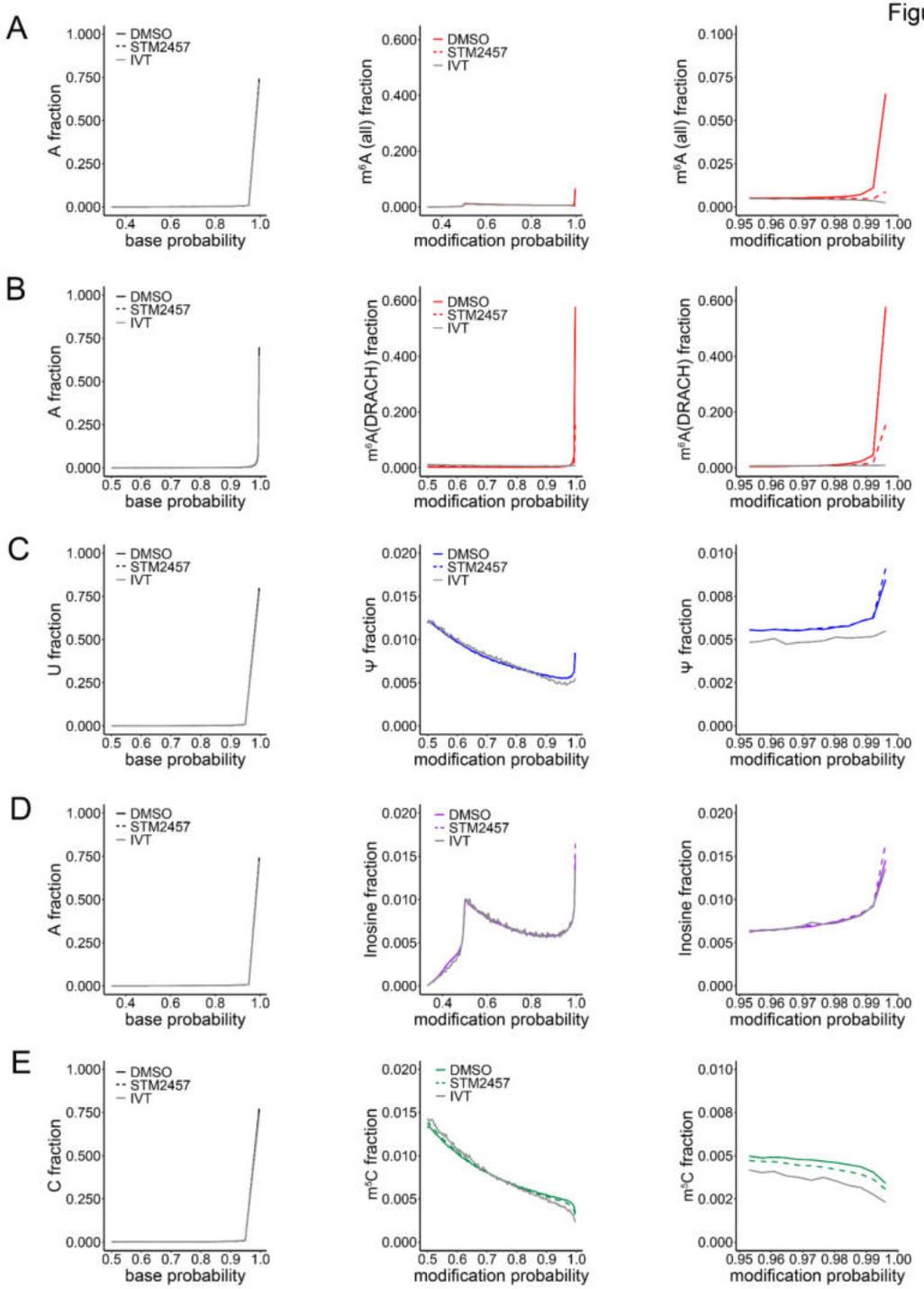
A
B
C
D
E
DMSO
STM2457
IVT
A fraction
m6A (all) fraction
m6A(DRACH) fraction
U fraction
Ψ fraction
Inosine fraction
C fraction
m5C fraction
base probability
modification probability

Figure S4

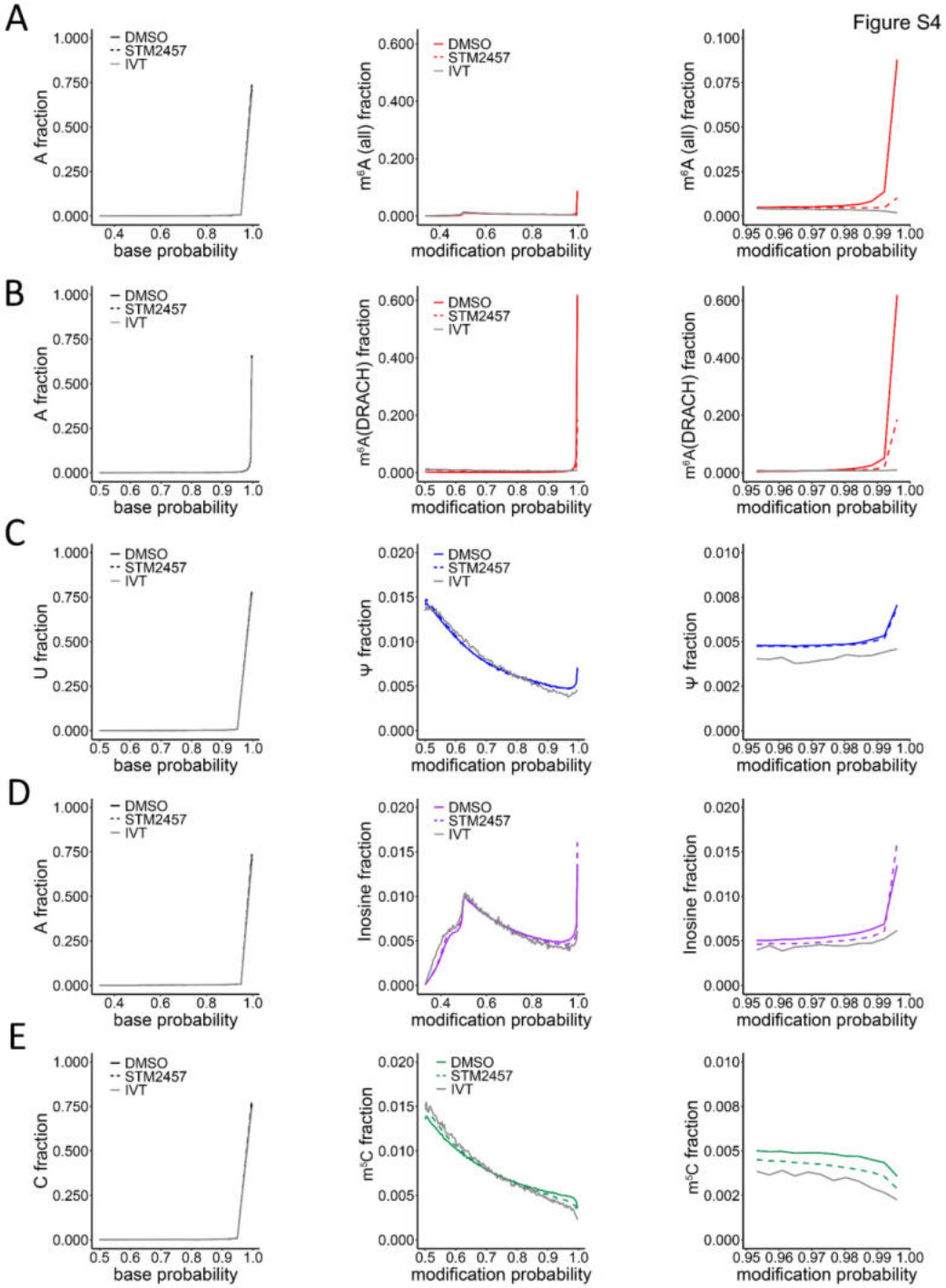
A
B
C
D
E
DMSO
STM2457
IVT
A fraction
m6A (all) fraction
m6A(DRACH) fraction
U fraction
Ψ fraction
Inosine fraction
C fraction
m5C fraction
base probability
modification probability

Figure S5

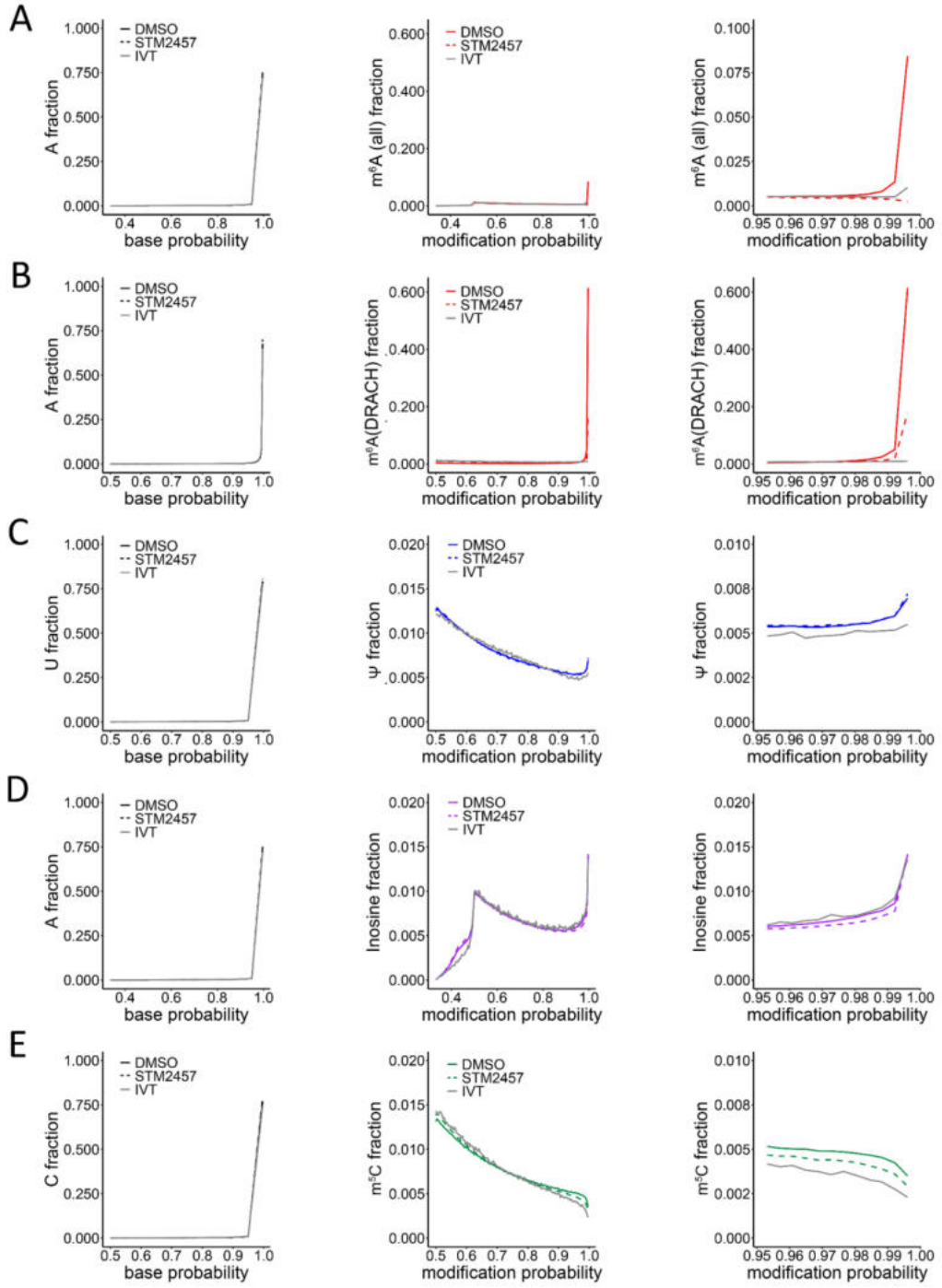
A
DMSO
STM2457
IVT
A fraction
base probability
m6A (all) fraction
modification probability
B
m6A(DRACH) fraction
C
U fraction
Ψ fraction
D
Inosine fraction
E
C fraction
m5C fraction

Figure S6

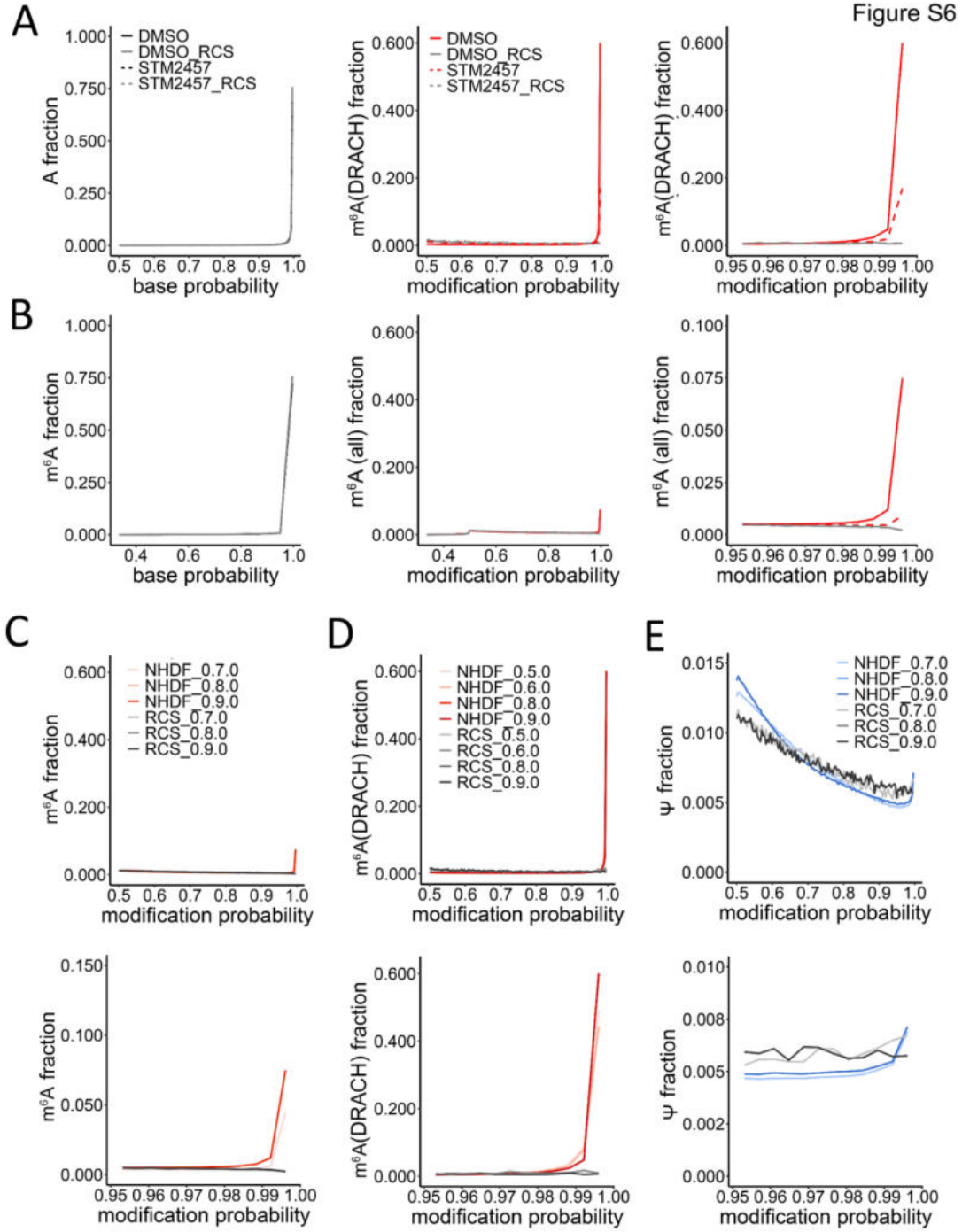
A
DMSO
DMSO_RCS
STM2457
STM2457_RCS
A fraction
base probability
m6A(DRACH) fraction
modification probability
B
m6A fraction
m6A (all) fraction
C
NHDF_0.7.0
NHDF_0.8.0
NHDF_0.9.0
RCS_0.7.0
RCS_0.8.0
RCS_0.9.0
D
NHDF_0.5.0
NHDF_0.6.0
RCS_0.5.0
RCS_0.6.0
E
ψ fraction

Figure S7

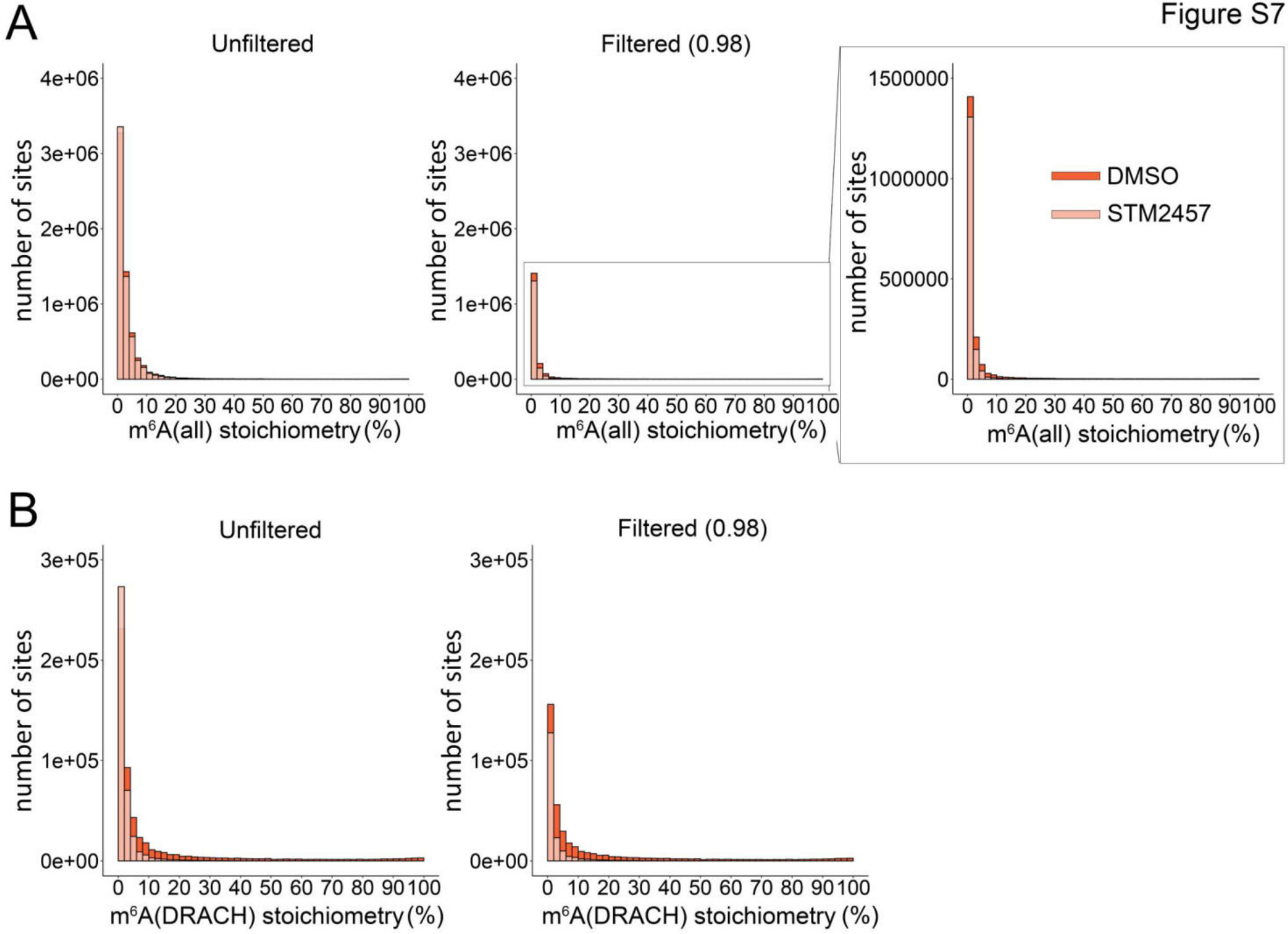
A
Unfiltered
Filtered (0.98)
number of sites
4e+06
3e+06
2e+06
1e+06
0e+00
1500000
1000000
500000
0
0 10 20 30 40 50 60 70 80 90 100
m6A(all) stoichiometry (%)
DMSO
STM2457
B
3e+05
2e+05
1e+05
m6A(DRACH) stoichiometry (%)

Figure S8

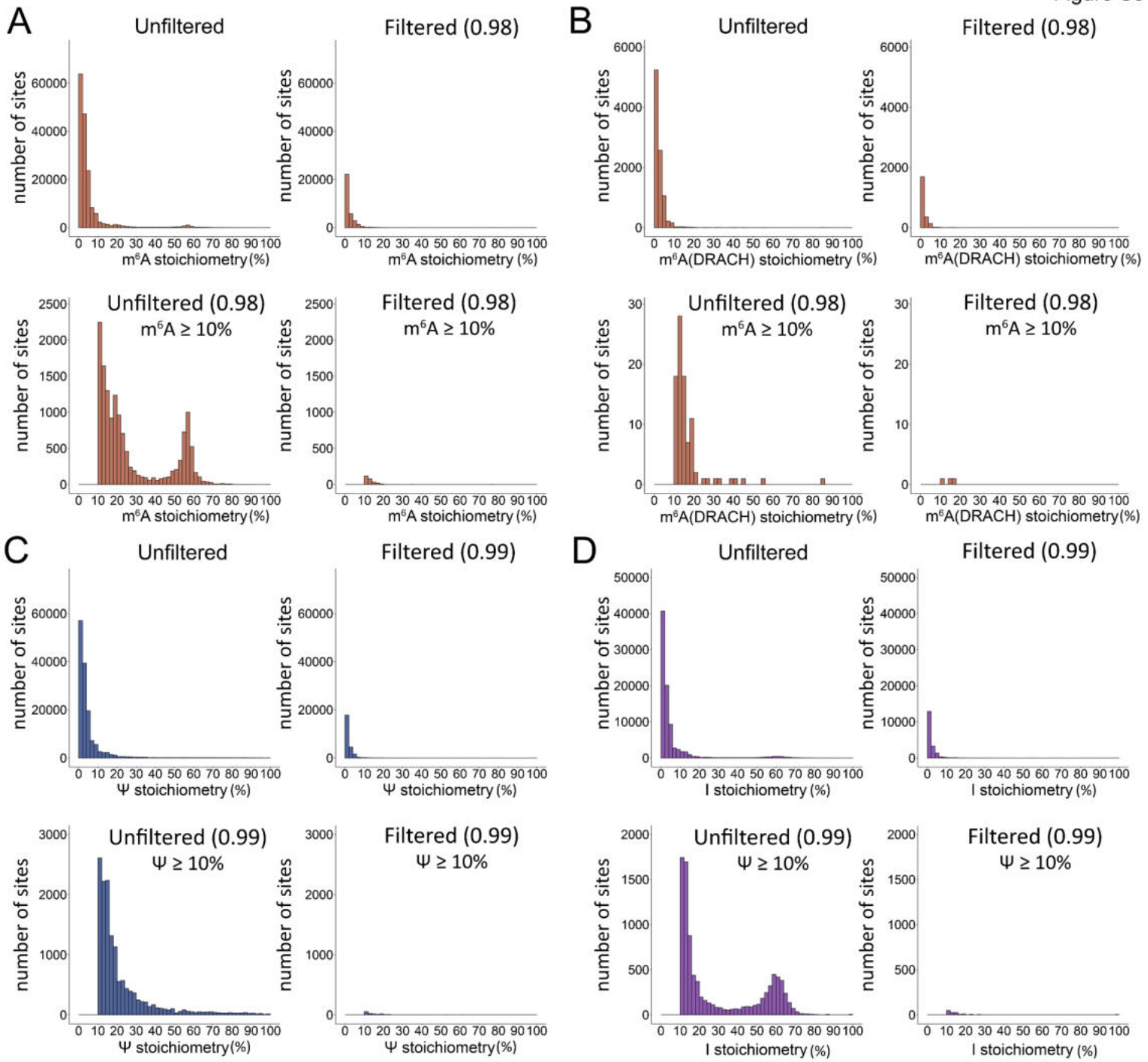
A
Unfiltered
Filtered (0.98)
Unfiltered (0.98)
m6A ≥ 10%
Filtered (0.98)
m6A ≥ 10%
number of sites
m6A stoichiometry (%)
B
Unfiltered
Filtered (0.98)
Unfiltered (0.98)
m6A ≥ 10%
Filtered (0.98)
m6A ≥ 10%
number of sites
m6A(DRACH) stoichiometry (%)
C
Unfiltered
Filtered (0.99)
Unfiltered (0.99)
Ψ ≥ 10%
Filtered (0.99)
Ψ ≥ 10%
number of sites
Ψ stoichiometry (%)
D
Unfiltered
Filtered (0.99)
Unfiltered (0.99)
Ψ ≥ 10%
Filtered (0.99)
Ψ ≥ 10%
number of sites
I stoichiometry (%)

Figure S9

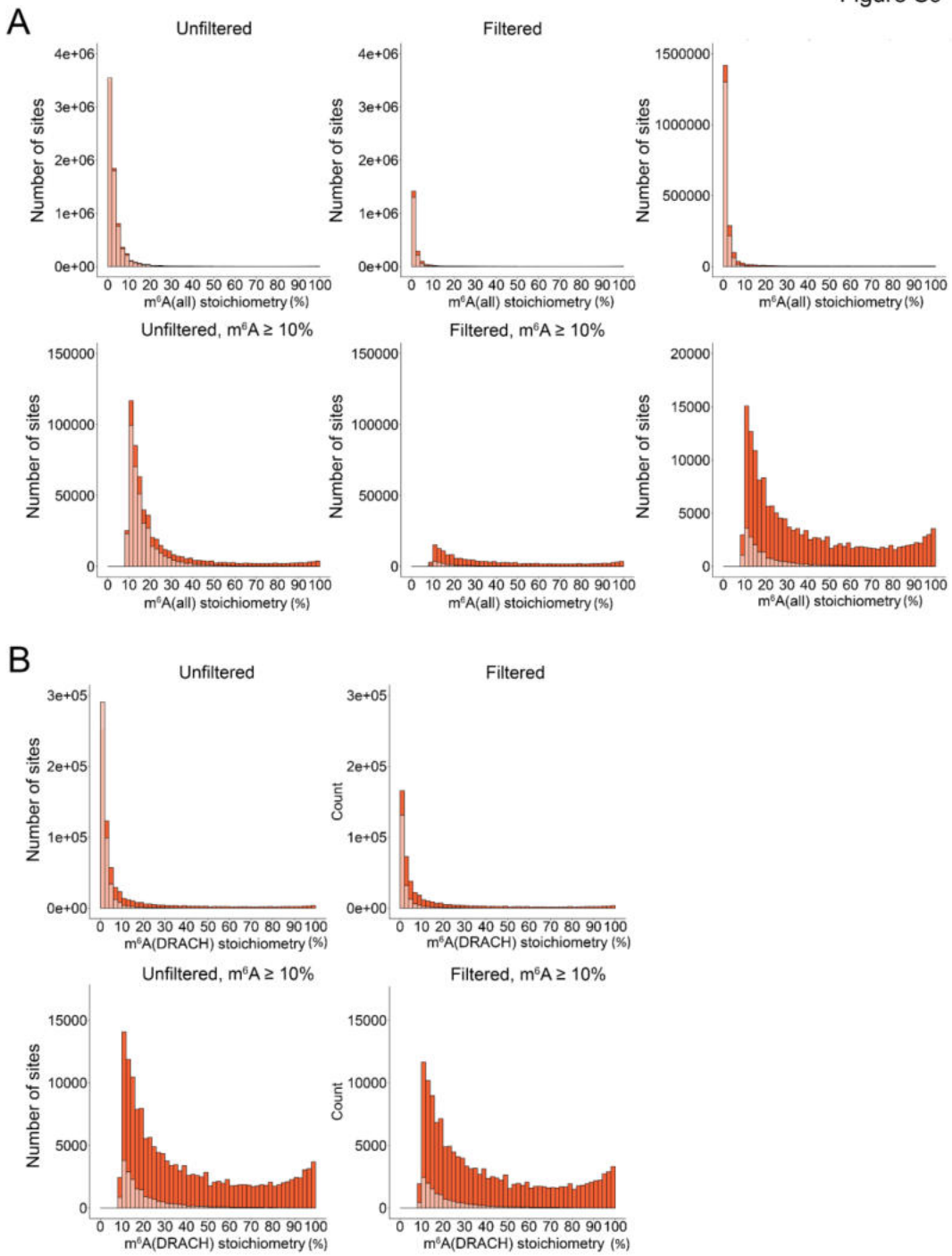
A
Unfiltered
Filtered
Unfiltered, m6A ≥ 10%
Filtered, m6A ≥ 10%
Number of sites
m6A(all) stoichiometry (%)
B
Unfiltered
Filtered
Unfiltered, m6A ≥ 10%
Filtered, m6A ≥ 10%
Number of sites
Count
m6A(DRACH) stoichiometry (%)

Figure S10

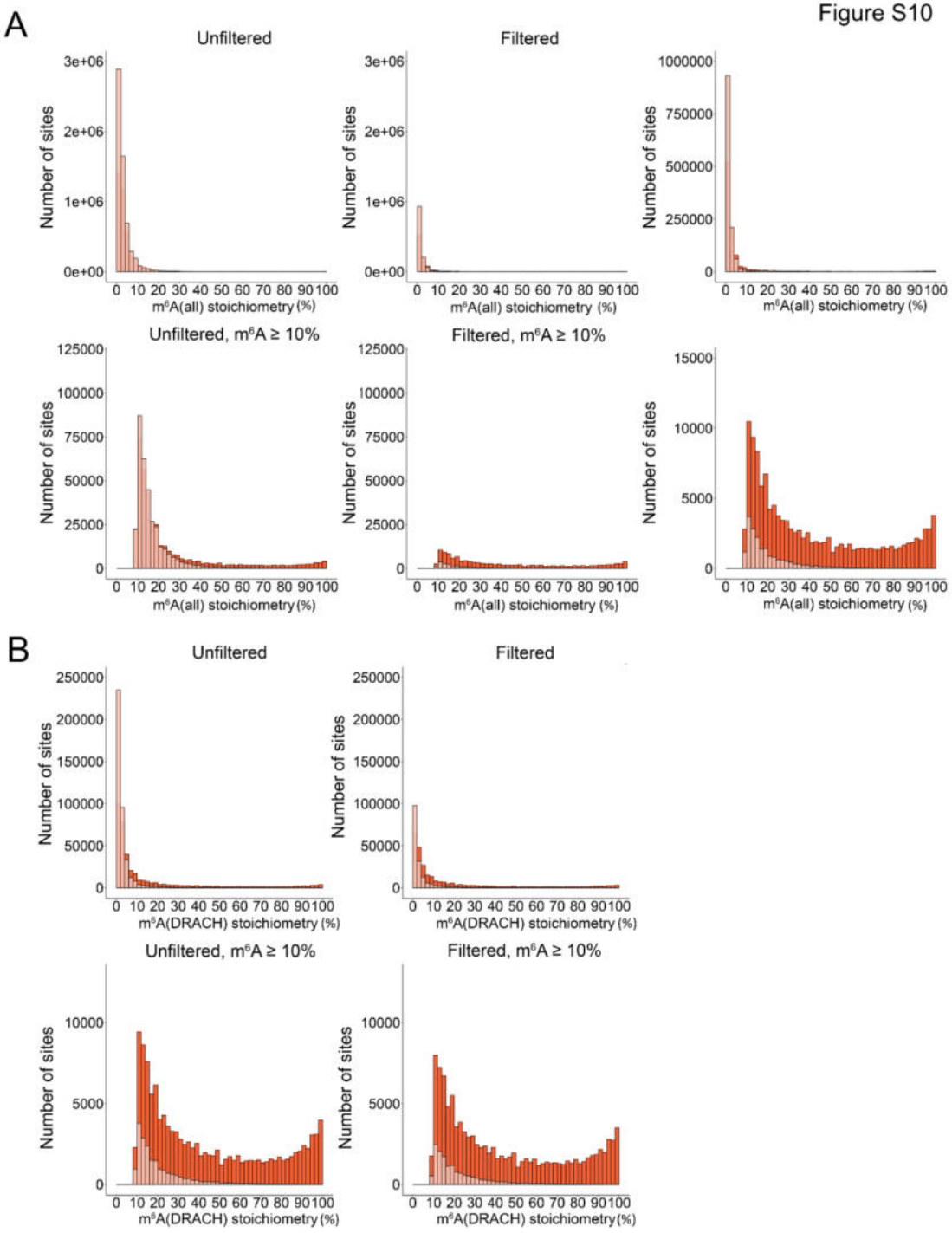
A
Unfiltered
Filtered
Unfiltered, m6A ≥ 10%
Filtered, m6A ≥ 10%
Number of sites
m6A(all) stoichiometry (%)
B
Unfiltered
Filtered
Unfiltered, m6A ≥ 10%
Filtered, m6A ≥ 10%
Number of sites
m6A(DRACH) stoichiometry (%)

Figure S11

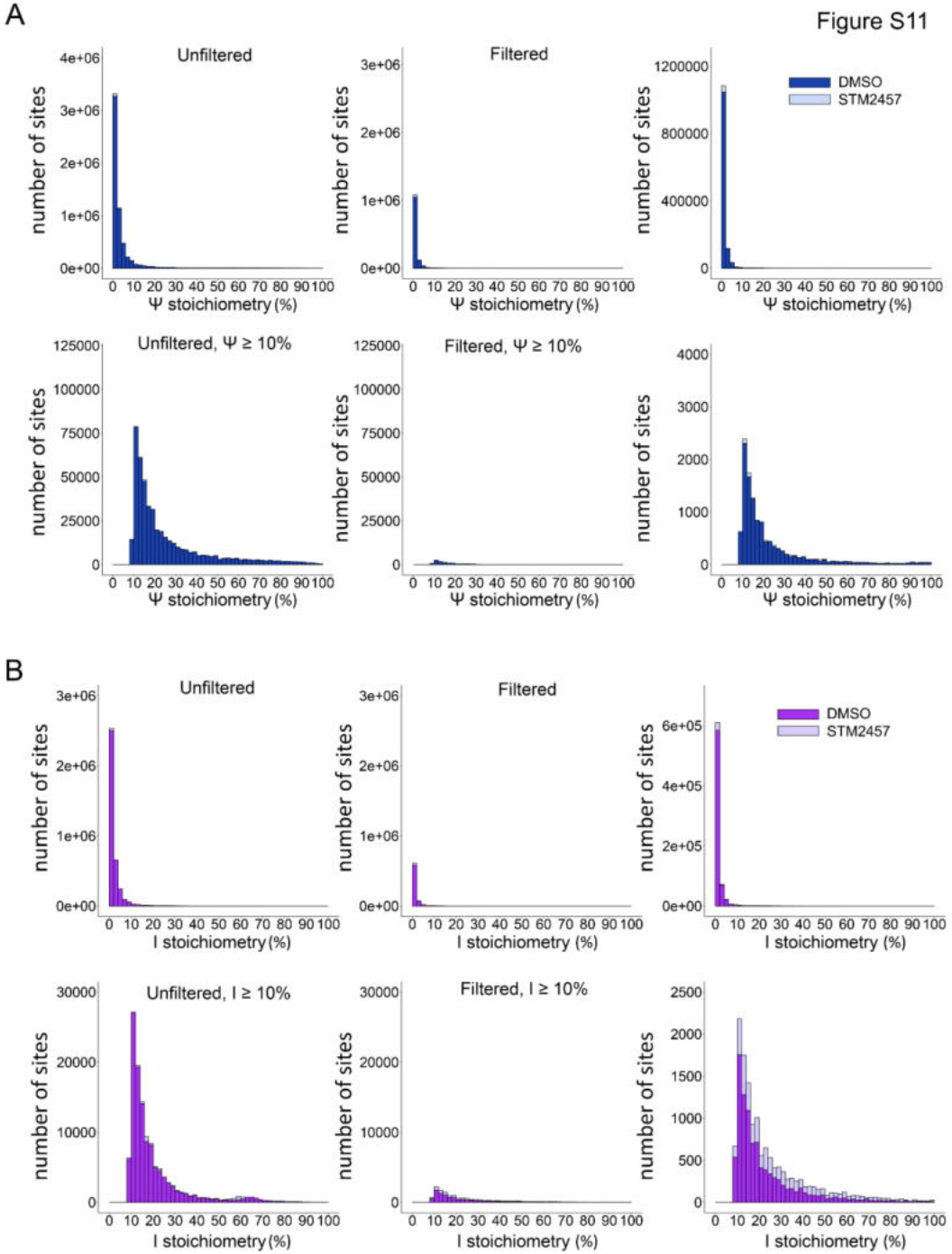
A
Unfiltered
Filtered
DMSO
STM2457
number of sites
Ψ stoichiometry (%)
Unfiltered, Ψ ≥ 10%
Filtered, Ψ ≥ 10%
B
I stoichiometry (%)
Unfiltered, I ≥ 10%
Filtered, I ≥ 10%

Figure S12

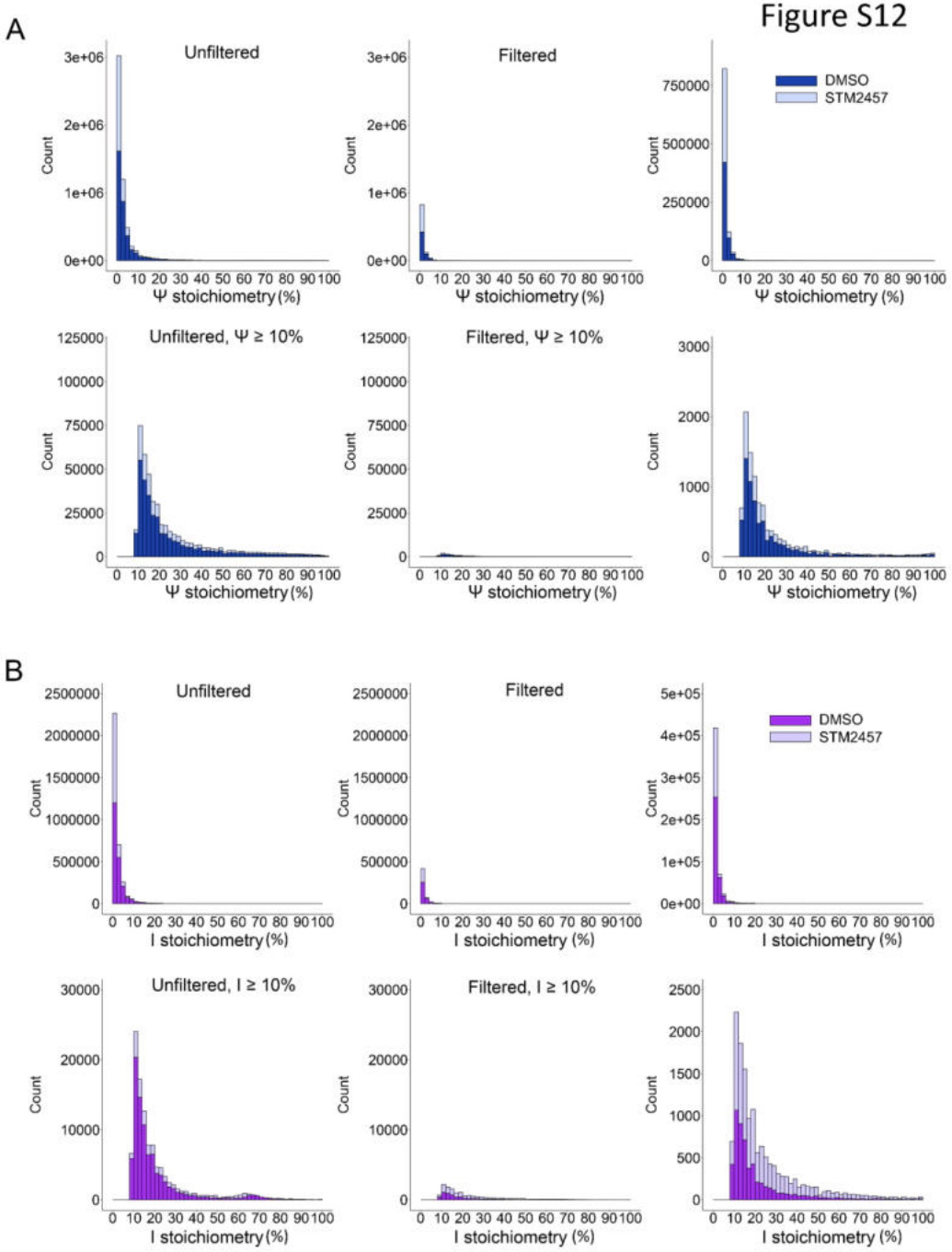
A
Unfiltered
Filtered
DMSO
STM2457
Unfiltered, Ψ ≥ 10%
Filtered, Ψ ≥ 10%
Count
Ψ stoichiometry (%)
B
Unfiltered
Filtered
DMSO
STM2457
Unfiltered, I ≥ 10%
Filtered, I ≥ 10%
Count
I stoichiometry (%)

Figure S13

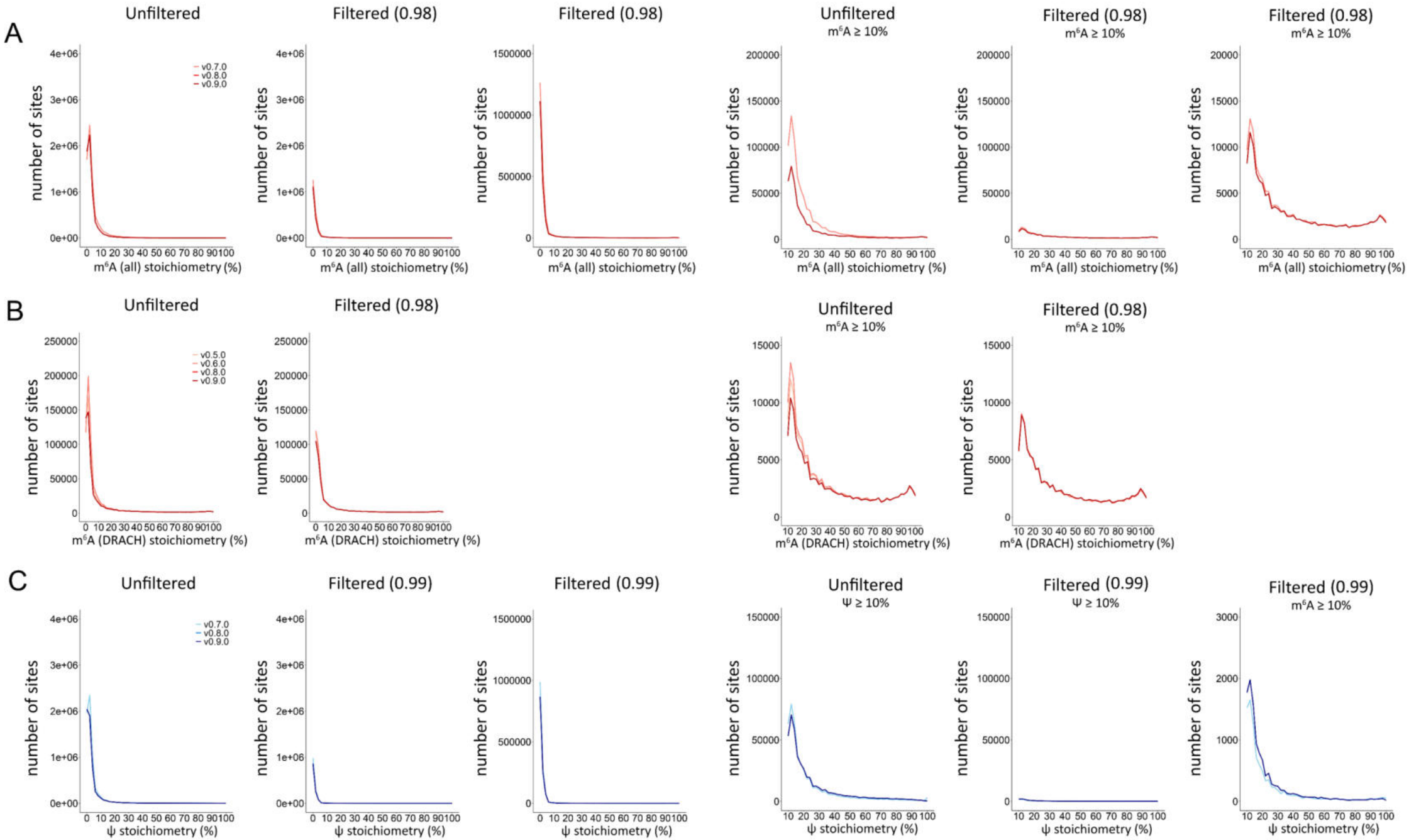
A
Unfiltered
Filtered (0.98)
Filtered (0.98)
Unfiltered
m6A ≥ 10%
Filtered (0.98)
m6A ≥ 10%
Filtered (0.98)
m6A ≥ 10%
v0.7.0
v0.8.0
v0.9.0
number of sites
m6A (all) stoichiometry (%)
B
Unfiltered
Filtered (0.98)
Unfiltered
m6A ≥ 10%
Filtered (0.98)
m6A ≥ 10%
v0.5.0
v0.6.0
v0.8.0
v0.9.0
number of sites
m6A (DRACH) stoichiometry (%)
C
Unfiltered
Filtered (0.99)
Filtered (0.99)
Unfiltered
Ψ ≥ 10%
Filtered (0.99)
Ψ ≥ 10%
Filtered (0.99)
m6A ≥ 10%
v0.7.0
v0.8.0
v0.9.0
number of sites
ψ stoichiometry (%)

Figure S14

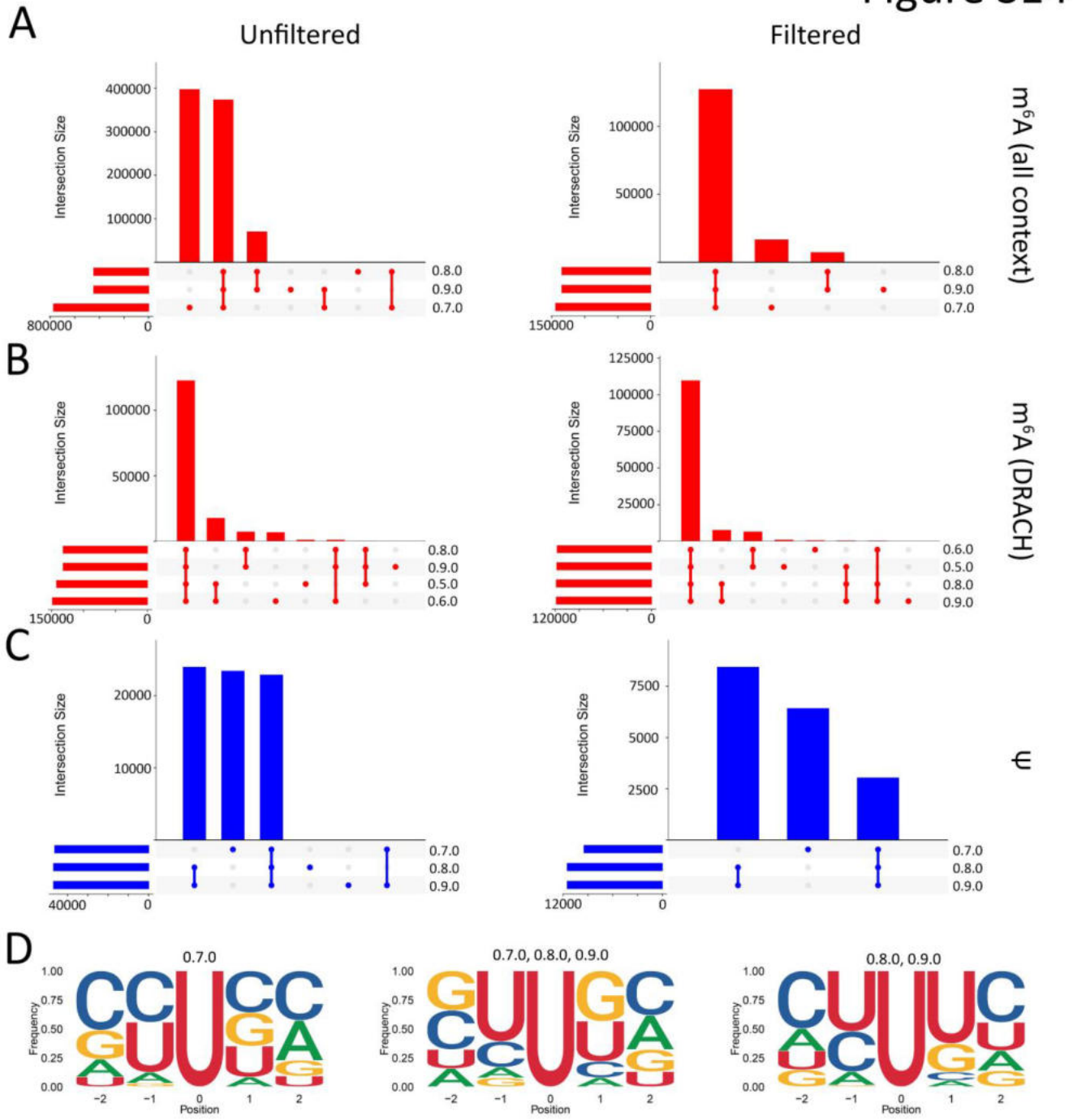
A
Unfiltered
Filtered
m6A (all context)
Intersection Size
400000
300000
200000
100000
800000
0
0.8.0
0.9.0
0.7.0
150000
B
m6A (DRACH)
125000
75000
50000
25000
120000
0.6.0
0.5.0
C
Ψ
20000
10000
7500
5000
2500
40000
12000
D
0.7.0
0.7.0, 0.8.0, 0.9.0
0.8.0, 0.9.0
Frequency
Position

Figure S15

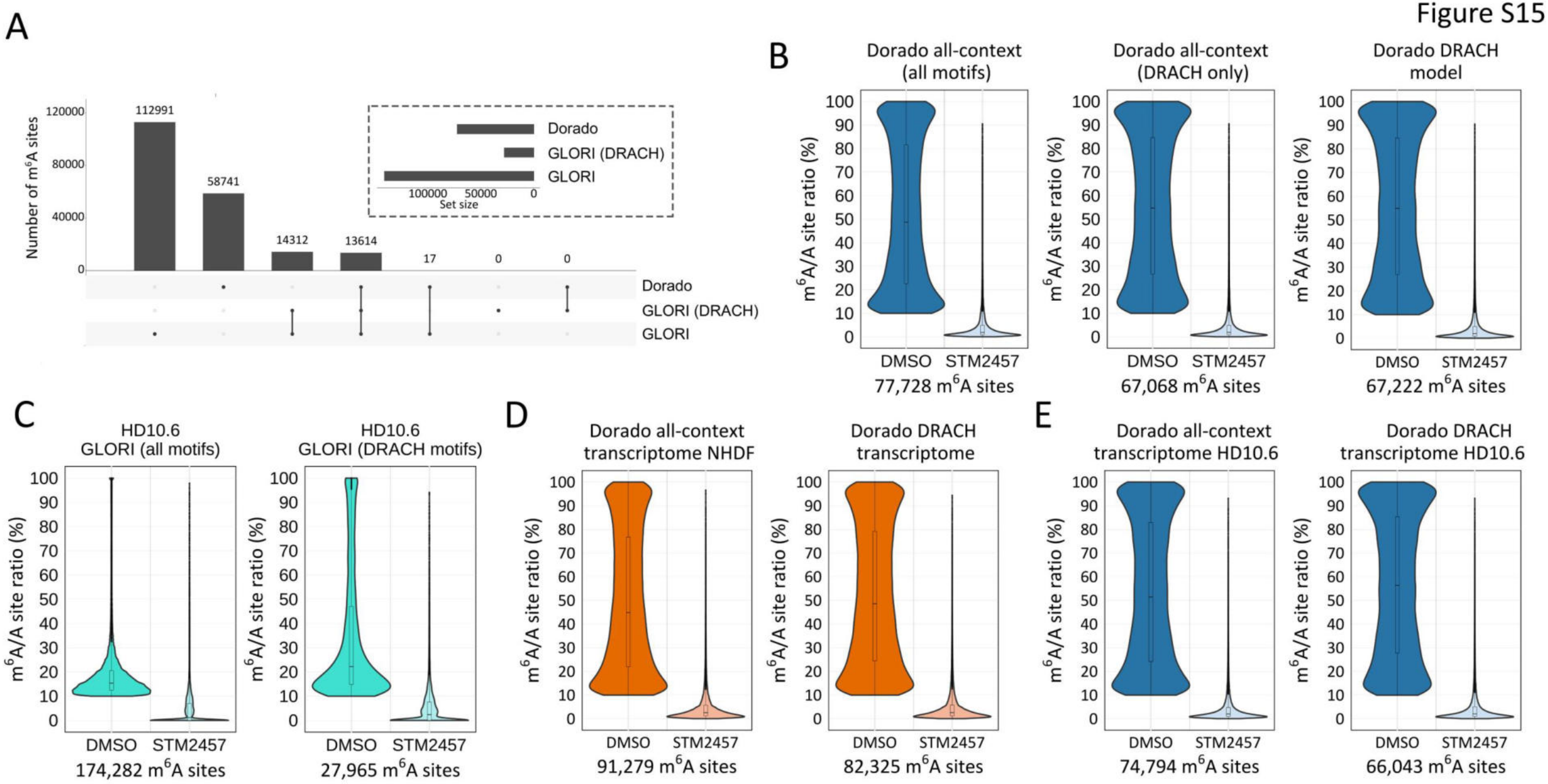
A
Number of m6A sites
120000
80000
40000
0
112991
58741
14312
13614
17
0
0
Dorado
GLORI (DRACH)
GLORI
100000
50000
0
Set size
B
Dorado all-context (all motifs)
Dorado all-context (DRACH only)
Dorado DRACH model
m6A/A site ratio (%)
DMSO
STM2457
77,728 m6A sites
67,068 m6A sites
67,222 m6A sites
C
HD10.6 GLORI (all motifs)
HD10.6 GLORI (DRACH motifs)
174,282 m6A sites
27,965 m6A sites
D
Dorado all-context transcriptome NHDF
Dorado DRACH transcriptome
91,279 m6A sites
82,325 m6A sites
E
Dorado all-context transcriptome HD10.6
Dorado DRACH transcriptome HD10.6
74,794 m6A sites
66,043 m6A sites

Figure S16

A

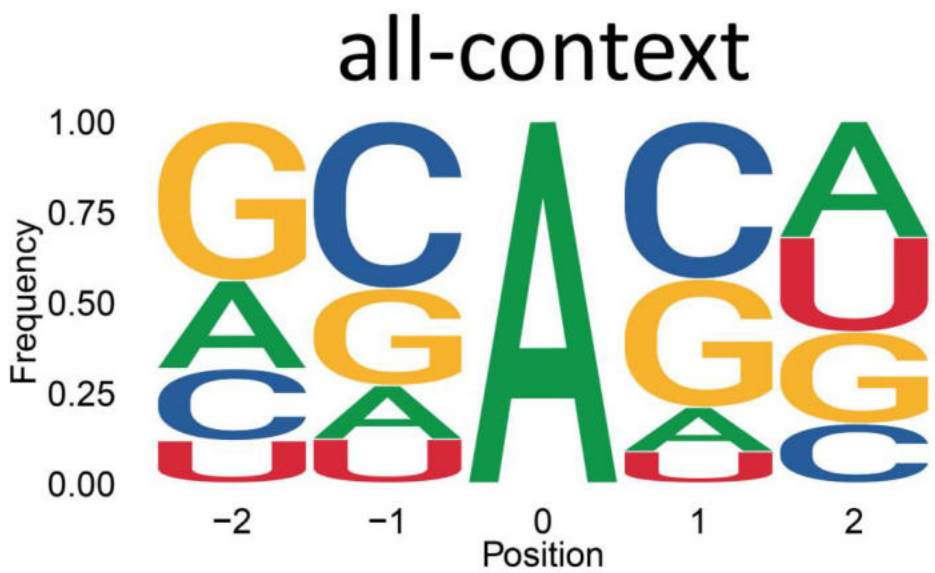

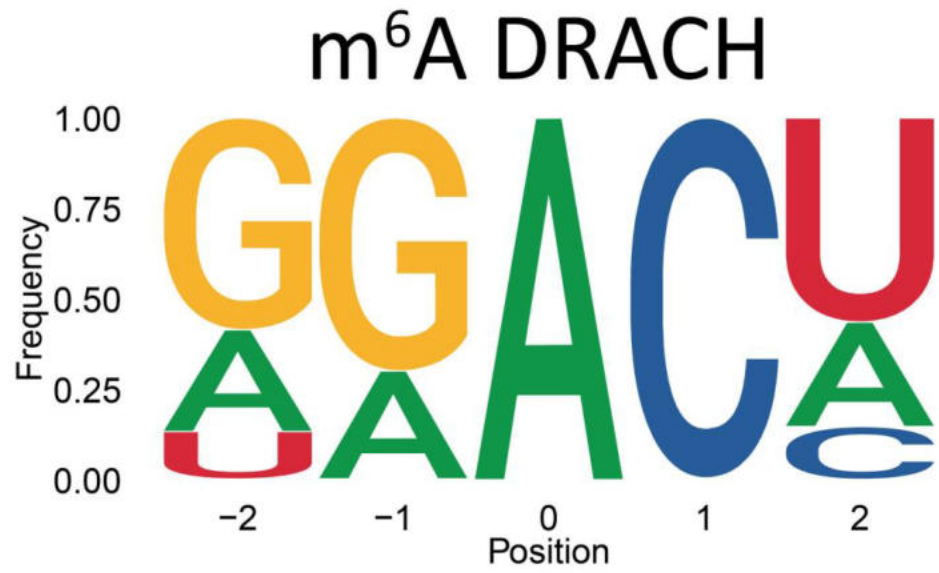

NHDF

B

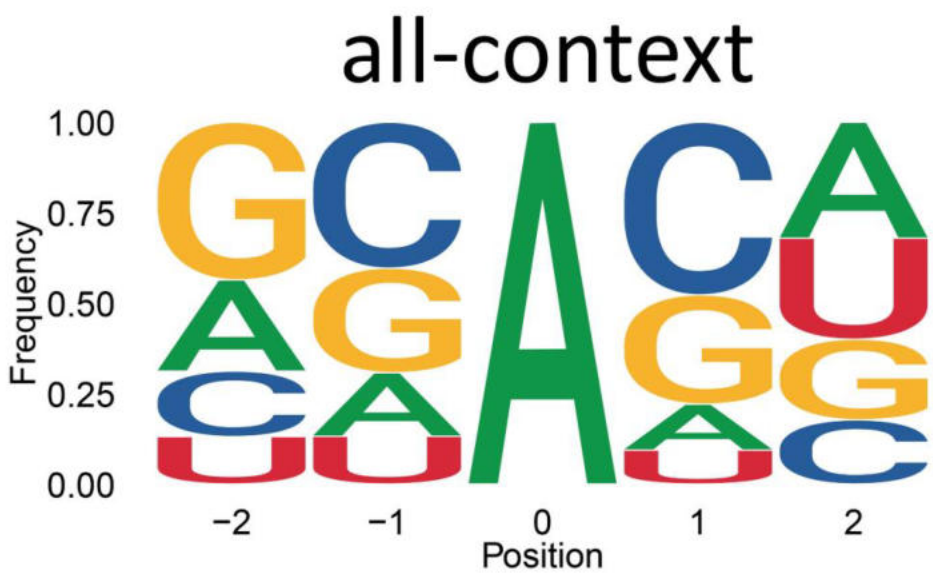

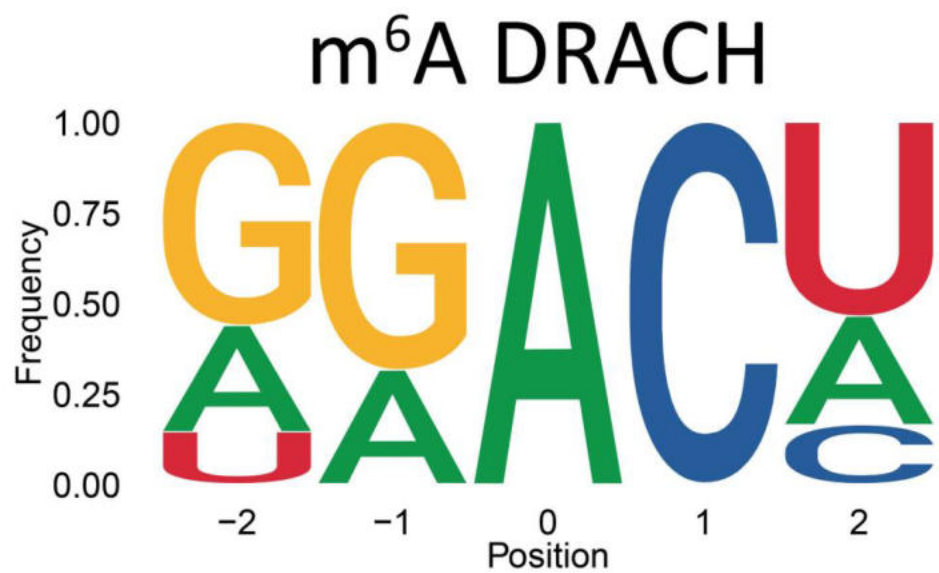

HD10.6

Figure S17

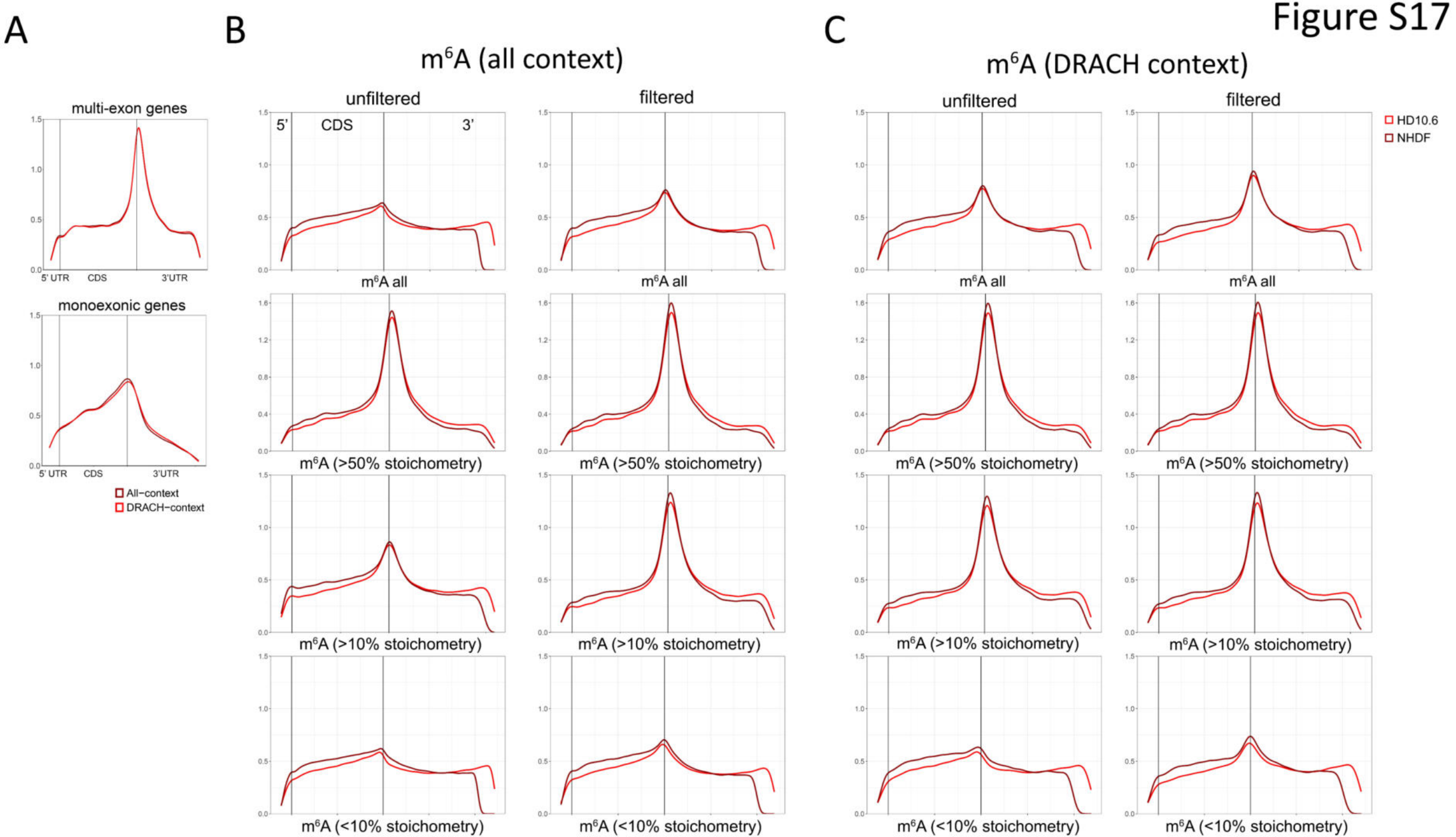
A
multi-exon genes
5' UTR
CDS
3'UTR
monoexonic genes
All−context
DRACH−context
B
m6A (all context)
unfiltered
filtered
5'
CDS
3'
m6A all
m6A (>50% stoichometry)
m6A (>10% stoichometry)
m6A (<10% stoichometry)
C
m6A (DRACH context)
HD10.6
NHDF